Comparison of aqueous SOA product distributions from guaiacol oxidation by non-phenolic and phenolic methoxybenzaldehydes as photosensitizers in the absence and presence of ammonium nitrate

Beatrix Rosette Go Mabato[1,2], Yong Jie Li[3], Dan Dan Huang[4], Yalin Wang[3], and Chak K. Chan[1,2]*

[1]School of Energy and Environment, City University of Hong Kong, Hong Kong, China
[2]City University of Hong Kong Shenzhen Research Institute, Shenzhen, China
[3]Department of Civil and Environmental Engineering, and Centre for Regional Ocean, Faculty of Science and Technology, University of Macau, Macau, China
[4]Shanghai Academy of Environmental Sciences, Shanghai 200233, China

Correspondence to: Chak K. Chan (Chak.K.Chan@cityu.edu.hk)

Abstract. Aromatic carbonyls (e.g., methoxybenzaldehydes), an important class of photosensitizers, are abundant in the atmosphere. Photosensitization and nitrate-mediated photo-oxidation can occur simultaneously, yet studies about their interactions, particularly for aqueous secondary organic aerosol (aqSOA) formation, remain limited. This study compared non-phenolic (3,4-dimethoxybenzaldehyde, DMB) and phenolic (vanillin, VL) methoxybenzaldehydes as photosensitizers for aqSOA formation via guaiacol (GUA) oxidation in the absence and presence of ammonium nitrate (AN) under atmospherically relevant cloud and fog conditions. GUA oxidation by triplet excited states of DMB (^{3}DMB*) (GUA+DMB) was ~4 times faster and exhibited greater light absorption than oxidation by ^{3}VL* (GUA+VL). Both GUA+DMB and GUA+VL formed aqSOA composed of oligomers, functionalized monomers, oxygenated ring-opening species, and N-containing products in the presence of AN. The observation of N-heterocycles such as imidazoles indicates the participation of ammonium in the reactions. The majority of generated aqSOA are potential brown carbon (BrC) chromophores. Oligomerization and functionalization dominated in GUA+DMB and GUA+VL, but functionalization appeared to be more important in GUA+VL due to contributions from VL itself. AN did not significantly affect the oxidation kinetics, but it had distinct effects on the product distributions, likely due to differences in the photosensitizing abilities and structural features of DMB and VL. In particular, the more extensive fragmentation in GUA+DMB than in GUA+VL likely generated more N-containing products in GUA+DMB+AN. In GUA+VL+AN, the increased oligomers may be due to VL-derived phenoxy radicals induced by ˙OH or ˙NO$_2$ from nitrate photolysis. Furthermore, increased nitrated products observed in the presence of both DMB or VL and AN than in AN alone implies that photosensitized reactions may promote nitration. This work demonstrates how the structural features of photosensitizers affect aqSOA formation via non-carbonyl phenol oxidation. Potential interactions between photosensitization and AN photolysis were also elucidated. These findings facilitate a better understanding of photosensitized aqSOA formation and highlight the importance of AN photolysis in these reactions.

1 Introduction

Photosensitized reactions involving triplet excited states of organic compounds ($^3C^*$) are efficient pathways for the formation of secondary organic aerosol in the aqueous phase (aqSOA; Smith et al., 2014, 2015, 2016; Yu et al., 2014, 2016; Chen et al., 2018; Lu et al., 2019; Ye et al., 2019; Chen et al., 2020; Liu et al., 2020; Jiang et al., 2021; Ma et al., 2021; Misovich et al., 2021; Ou et al., 2021; F. Li et al., 2022; X. Li et al., 2022; Aregahegn et al., 2022; Mabato et al., 2022; Wang et al., 2022). Upon irradiation by solar radiation, photosensitizers form an excited triplet state that directly reacts with substrates (e.g., phenols), and can generate singlet oxygen ($^1O_2$), superoxide ($O_2^{\bullet-}$) or hydroperoxyl ($^\bullet HO_2$) radicals, and hydroxyl radicals ($^\bullet OH$) upon reactions with O_2 and substrates (George et al., 2018; Chen et al., 2020), thereby facilitating the oxidation of rather volatile species and contributing to aqSOA formation. An important class of photosensitizers is aromatic carbonyls (e.g., methoxybenzaldehydes) which are abundant in aerosol particles, cloud waters, and fog waters (Anastasio et al., 1997; Felber et al., 2021). Aromatic carbonyls can be emitted from anthropogenic sources and biomass burning (BB; Lipari et al.,1984; Edye and Richards, 1991; Hawthorne et al., 1992; Simoneit et al., 1993, 1999; Anastasio et al., 1997; Felber et al., 2021), or formed via atmospheric oxidation of aromatic hydrocarbons (Hoshino et al., 1978; Calvert and Madronich, 1987; Anastasio et al., 1997; Felber et al., 2021). BB is also a significant source of phenols through lignin pyrolysis (Simpson et al., 2005). Phenolic carbonyls have a hydroxyl (–OH) group on the aromatic ring, whereas non-phenolic carbonyls do not. BB smoke has been reported to have comparable concentrations of phenolic and non-phenolic carbonyls (Simoneit et al., 1993; Anastasio et al., 1997).

Most previous studies on aqSOA formation via photosensitized non-carbonyl phenol oxidation have examined 3,4-dimethoxybenzaldehyde (DMB), a non-phenolic methoxybenzaldehyde, as the photosensitizer (Smith et al., 2014, 2015; Yu et al., 2014, 2016; Ye et al., 2019; Chen et al., 2020; Jiang et al., 2021; Ma et al., 2021; Misovich et al., 2021; Ou et al., 2021; X. Li et al., 2022). By contrast, phenolic carbonyls have been mainly studied as aqSOA precursors via $^\bullet OH$-, nitrate-, nitrite-, and $^3DMB^*$-mediated oxidation (Li et al., 2014; Huang et al., 2018; Pang et al., 2019; Jiang et al., 2021; Misovich et al., 2021). However, strongly light-absorbing phenolic carbonyls (e.g., molar absorptivity above 300 nm $\geq 7 \times 10^3$ M^{-1} cm^{-1}) can also serve as photosensitizers to promote aqSOA formation (Smith et al., 2016; Mabato et al., 2022). For instance, the direct photosensitized oxidation of phenolic carbonyls (i.e., oxidation of phenolic carbonyls by their $^3C^*$ or $^3C^*$-derived oxidants) such as vanillin (VL; another methoxybenzaldehyde) efficiently form low-volatility products, with aqSOA mass yields of up to 140% (Smith et al., 2016). Moreover, the aqSOA mass yields from the oxidation of syringol by $^3DMB^*$ and $^3VL^*$ are similar (111% and 114%, respectively; Smith et al., 2014, 2016). In addition, we recently reported that the direct photosensitized oxidation of VL and guaiacol oxidation by $^3VL^*$ yield similar products (oligomers, functionalized monomers, and oxygenated ring-opening products) as observed with $^3DMB^*$ (Yu et al., 2014; Mabato et al., 2022). Guaiacol is a non-carbonyl BB methoxyphenol with an emission rate from fireplace wood combustion in the range of 172 to 279 mg/kg (Schauer et al., 2001; Simoneit, 2002). The atmospheric reactivity of methoxyphenols has recently been reviewed (Liu et al., 2022). However, our previous experiments (Mabato et al., 2022) were performed at a concentration (0.1 mM VL)

65 higher than what was typically used for DMB (0.005 to 0.01 mM; Smith et al., 2014, 2015; Yu et al., 2014, 2016). Therefore,

66 direct comparisons between photosensitization by ^{3}DMB* and ^{3}VL* cannot be made. Despite the above findings, much is

67 still unknown about how aqSOA formation proceeds in systems using phenolic carbonyls as photosensitizers.

68 BB aerosols are typically internally mixed with other aerosol components, such as ammonium nitrate (AN;

69 Zielinski et al., 2020). Hence, aromatic carbonyls and phenols may coexist with AN in BB aerosols. Nitrate and ammonium

70 facilitate the formation of aqSOA and brown carbon (BrC) via a number of pathways. Nitrate photolysis can produce $^\bullet$OH

71 and nitrating agents (e.g., $^\bullet$NO$_2$; Minero et al., 2007; Huang et al., 2018; Mabato et al., 2022; Wang et al., 2022; Yang et al.,

72 2022), and ammonium reacts with carbonyls to yield N-containing heterocycles (e.g., imidazoles) and oligomers capable of

73 UV-Vis light absorption (De Haan et al., 2009, 2011; Nozière et al., 2009, 2010, 2018; Shapiro et al., 2009; Yu et al., 2011;

74 Lee et al., 2013; Powelson et al., 2014; Gen et al., 2018; Grace et al., 2019; Mabato et al., 2019). Furthermore, nitrate

75 photolysis may be an important process for SO$_2$ oxidation and SOA formation in the particle phase (Gen et al., 2019a,

76 2019b, 2022; Zhang et al., 2020, 2021, 2022), and it can potentially modify the morphology of atmospheric viscous particles

77 (Liang et al., 2021). Yet, understanding of the effects of inorganic nitrate on aqSOA formation remains limited. In addition,

78 aqSOA formation studies involving aromatic carbonyls and phenols have probed either photosensitization or nitrate-

79 mediated photo-oxidation, but these reactions can occur simultaneously. For instance, we previously reported nitrated

80 compounds, including a potential imidazole derivative from the direct photosensitized oxidation of VL in the presence of AN

81 (Mabato et al., 2022). Accordingly, investigations on reaction systems including both photosensitizers and AN may provide

82 further insights into the aqueous-phase processing of BB aerosols.

83 In this work, we compared aqSOA formation from photosensitized guaiacol (GUA) oxidation by ^{3}C* of non-

84 phenolic and phenolic methoxybenzaldehydes under identical conditions (simulated sunlight and concentration) relevant to

85 cloud and fog waters. The effects of AN on photosensitized aqSOA formation were also examined. In this study, the

86 dominant aqSOA precursor is GUA (Henry's law constant of 9.2×10^2 M atm^{-1}; Sagebiel et al., 1992), and DMB and VL

87 were used as photosensitizers to oxidize GUA. DMB and VL (Henry's law constants of 7.3×10^3 M atm^{-1} and 4.7×10^5 M

88 atm^{-1}, respectively; Yaws, 1994; EPI Suite version 4.1, 2012; Felber et al., 2021), which are also abundant in BB emissions

89 (Schauer et al., 2001; Li et al., 2014; Chen et al., 2017; Pang et al., 2019; Mabato et al., 2022) and whose structures differ

90 only by one functional group (–OCH$_3$ for the former and –OH for the latter, Fig. 1), represented non-phenolic and phenolic

91 methoxybenzaldehydes, respectively. The structures of GUA, DMB, and VL are provided in Figure 1. Based on their

92 quantum yield of ^{3}C* formation, DMB and VL have been classified as moderate and poor photosensitizers, respectively

93 (Felber et al., 2021). The photosensitized oxidation of GUA by ^{3}DMB* or ^{3}VL* in the absence (and presence) of AN are

94 referred to as GUA+DMB(+AN) and GUA+VL(+AN), respectively. GUA photo-oxidation by AN alone (GUA+AN) was

95 also explored for comparison with GUA+DMB+AN and GUA+VL+AN. The molar absorptivities of GUA, DMB, VL, and

96 nitrate are shown in Figure 1. The precursor and photosensitizer decay kinetics, detected products, and absorbance

97 enhancement were used to characterize the reactions. However, it should be noted that we mainly focused on the analyses of

98 the reaction products and product distribution.

99   While several studies on photo-oxidation of BB emissions are available, this work focuses on the comparison

100   between non-phenolic and phenolic methoxybenzaldehydes as photosensitizers in the absence and presence of AN for

101   aqSOA formation. We found that GUA oxidation by ^{3}DMB* was faster and exhibited greater light absorption relative to

102   GUA+VL. These are likely attributed to the stronger photosensitizing ability of DMB and the –OH group of VL, making it

103   more prone to oxidation and more reactive towards electrophilic aromatic substitution. Oligomerization and functionalization

104   dominated in GUA+DMB and GUA+VL, but functionalization appeared to be more significant in GUA+VL due to VL

105   transformation products. Although AN did not significantly influence the oxidation kinetics due to the predominant role of

106   photosensitizer chemistry compared to nitrate, AN promoted the formation of N-containing products. These include N-

107   heterocycles (e.g., imidazoles), suggesting the participation of ammonium in the reactions. Moreover, the product

108   distributions indicate distinct interactions between photosensitization by ^{3}DMB* and ^{3}VL* and AN photolysis. In particular,

109   AN generated more N-containing products in GUA+DMB+AN than in GUA+VL+AN, and increased the oligomers in

110   GUA+VL+AN. Furthermore, increased nitrated compounds in GUA+DMB+AN and GUA+VL+AN compared to GUA+AN

111   suggest that photosensitized reactions may promote reactions by nitrate photolysis.

112   **2 Methods**

113   **2.1 Aqueous phase photo-oxidation experiments**

114   Procedures for the photo-oxidation experiments are presented in detail in our previous study (Mabato et al., 2022).

115   Experimental solutions were prepared using 0.1 mM guaiacol (GUA, Sigma Aldrich, ≥98.0%) and 0.01 mM 3,4-

116   dimethoxybenzaldehyde (DMB, Acros Organics, 99+%) or 0.01 mM vanillin (VL, Acros Organics, 99%, pure), in the

117   absence and presence of ammonium nitrate (1 mM; AN, Acros Organics, 99+%, for analysis). These GUA and

118   methoxybenzaldehydes concentrations are within the values expected in cloud or fog drops in areas with significant wood

119   combustion (Anastasio et al., 1997; Rogge et al., 1998; Nolte et al., 2001). The AN concentration represents values usually

120   observed in cloud and fog waters (Munger et al., 1983; Collett et al., 1998; Zhang and Anastasio, 2003; Li et al., 2011;

121   Giulianelli et al., 2014; Bianco et al., 2020). It must be noted that this study did not intend to identify the AN concentrations

122   that would affect the kinetics but attempted to analyze the effects of AN on photosensitized aqSOA formation. A solution

123   composed of 0.1 mM GUA and 1 mM AN (GUA+AN) was also examined for comparison with GUA+DMB+AN and

124   GUA+VL+AN. Sulfuric acid (H_2SO_4; Acros Organics, ACS reagent, 95% solution in water) was used to adjust the pH of the

125   solutions to 4, which is within typical cloud pH values (2–7; Pye et al., 2020) and pH values observed in wood burning-

126   impacted cloud and fog waters (Collett et al., 1998; Raja et al., 2008). The solutions (initial volume of 500 mL) were

127   bubbled with synthetic air (0.5 dm^3/min) for 30 min before irradiation and throughout the reactions to achieve air-saturated

128   conditions (Du et al., 2011; Chen et al., 2020) and were continuously magnetically stirred. In this study, the reactions can

129   generate ^{3}DMB*/^{3}VL* and secondary oxidants ($^1O_2$, $O_2^{\cdot-}/^{\cdot}HO_2$, $^{\cdot}OH$) but not ozone. Solutions contained in a quartz

130   photoreactor were irradiated using a xenon lamp (model 6258, Ozone free xenon lamp, 300 W, Newport) equipped with a

131 longpass filter (20CGA-305 nm cut-on filter, Newport) to eliminate light below 300 nm. The reaction temperatures were

132 maintained at 27 ± 2 °C using cooling fans positioned around the photoreactor and lamp housing. The averaged initial

133 photon flux in the reactor measured from 300 to 380 nm was $\sim 3 \times 10^{15}$ photons cm^{-2} s^{-1} nm^{-1} (Fig. 1), similar to our previous

134 work (Mabato et al., 2022). Samples were collected every 30 min for 180 min for offline analyses of (1) GUA, DMB, and

135 VL concentrations using ultra-high-performance liquid chromatography with photodiode array detector (UHPLC-PDA) and

136 (2) absorbance measurements using UV-Vis spectrophotometry. Moreover, the samples collected before and after irradiation

137 (180 min) were analyzed for (3) reaction products using UHPLC coupled with heated electrospray ionization Orbitrap mass

138 spectrometry (UHPLC-HESI-Orbitrap-MS) operated in positive and negative ion modes and (4) concentrations of small

139 organic acids using ion chromatography (IC). Each experiment was repeated independently at least three times. The reported

140 decay rate constants, small organic acids concentration, and absorbance enhancement were averaged from triplicate

141 experiments, and the corresponding errors represent one standard deviation. The pseudo-first-order rate constant (k') for

142 GUA decay was determined using the following equation (Huang et al., 2018):

$$ln\,([GUA]_t/[GUA]_0) = -k't \qquad \text{(Eq. 1)}$$

144 where $[GUA]_t$ and $[GUA]_0$ are GUA concentrations at time t and 0, respectively. DMB or VL decay rate constants were

145 calculated by replacing GUA with DMB or VL in Eq. 1. The decay rate constants were normalized to the photon flux

146 measured for each experiment through dividing k' by the measured 2-nitrobenzaldehyde (2NB; a chemical actinometer)

147 decay rate constant, j(2NB) (Mabato et al., 2022). In addition, the decay rate constants were corrected for the internal light

148 screening due to DMB, VL, and AN (Leifer, 1988; Zhang and Anastasio, 2003; Smith et al., 2014, 2015, 2016). The values

149 of the internal light screening factor (S_λ) determined around the peak in the light absorption action spectrum (DMB: 310-335

150 nm, VL: 304-364 nm, nitrate: 300-331 nm) (Smith et al., 2014, 2015, 2016) for an 8.5 cm cell were 0.95 for GUA+AN, 0.51

151 for GUA+DMB, 0.54 for GUA+DMB+AN, 0.57 for GUA+VL, and 0.59 for GUA+VL+AN. Moreover, two independently

152 prepared samples for each reaction condition were analyzed using UHPLC-HESI-Orbitrap-MS. Only peaks that were

153 reproducibly detected in both sets of samples were considered. For clarity, the formulas discussed in this work correspond to

154 neutral analytes (e.g., with H$^+$ or NH$_4^+$ removed from the ion formula). The details of the analytical procedures are provided

155 in the Supplement (Sects. S1 to S4).

2.2 Calculation of normalized abundance of products

157 Several recent studies have used comparisons of relative abundance of products based on peak areas from mass spectrometry

158 (MS) results (e.g., Lee et al., 2014; Romonosky et al., 2017; Wang et al., 2017; Fleming et al., 2018; Song et al., 2018; Klodt

159 et al., 2019; Ning et al., 2019) to show the relative importance of different types of compounds (K. Wang et al., 2021).

160 However, comparisons of relative abundance among different compounds can be subject to uncertainties as ionization

161 efficiencies in soft ionization, such as ESI, may significantly vary between different compounds (Kebarle, 2000; Schmidt et

162 al., 2006; Leito et al., 2008; Perry et al., 2008; Kruve et al., 2014). In our previous work (Mabato et al., 2022), we introduced

163 the normalized abundance of products ([P], unitless) (Eq. 2) as a semi-quantitative analysis that gives an overview of how

164 the signal intensities changed under different experimental conditions but not the quantification of the absolute product

165 concentration. The calculation assumes equal ionization efficiencies of different compounds, which is commonly used to

166 estimate O:C ratios of SOA (Bateman et al., 2012; Lin et al., 2012; Laskin et al., 2014; De Haan et al., 2019):

167

168
$$[P] = \frac{A_{P,t}}{A_{GUA,t}} \cdot \frac{[GUA]_t}{[GUA]_0}$$
(Eq. 2)

169 where $A_{P,t}$ and $A_{GUA,t}$ are the extracted ion chromatogram (EIC) peak areas of the product P and GUA from UHPLC-HESI-

170 Orbitrap-MS analyses at time t, respectively; $[GUA]_t$ and $[GUA]_0$ are the GUA concentrations (μM) determined using

171 UHPLC-PDA at time t and 0, respectively. Note that the normalized abundance of products has intrinsic uncertainties due to

172 the variability in ionization efficiencies for various compounds. Moreover, it should be noted that the normalized abundance

173 of products was calculated using only the positive ion mode data as the GUA signal from the negative ion mode was weak

174 and thus may present large uncertainties during normalization. Therefore, products that may not give signals or may have

175 weak signals in the positive ion mode were possibly underestimated in the normalized product abundance. Nevertheless, it

176 enables the comparison of MS results among different experiments. As demonstrated in our previous work (Mabato et al.,

177 2022) and the current study, a higher normalized abundance of products generally correlates with higher efficiency of

178 oxidation. The reported uncertainties were propagated from the changes in [GUA] measured using UHPLC-PDA and the MS

179 signal intensities.

180

181 3 Results and Discussion

182 Using kinetics data, MS analyses, and absorbance enhancement data, we first examined the differences between GUA+DMB

183 and GUA+VL (Sect. 3.1). Then, we analyzed GUA+DMB+AN, GUA+VL+AN, and GUA+AN (Sect. 3.2) to explore the

184 effects of nitrate photolysis and ammonium on photosensitized aqSOA formation.

185 3.1 Comparison of photosensitized GUA oxidation by non-phenolic (^{3}DMB*) and phenolic (^{3}VL*)
186 methoxybenzaldehydes

187 Prior studies have reported that photosensitized non-carbonyl phenol oxidation in the presence of 3,4-

188 dimethoxybenzaldehyde (DMB) and vanillin (VL) (separately) was mainly driven by ^{3}DMB* and ^{3}VL*, respectively (Smith

189 et al., 2014; Mabato et al., 2022), while contributions from secondary oxidants such as $^1O_2$ and $^{\bullet}OH$ were likely minor.

190 However, both ^{3}DMB* and ^{3}VL* are efficiently quenched by O_2, suggesting that energy transfer should be considered in

191 evaluating photosensitized processes involving these methoxybenzaldehydes (Felber et al., 2021). Moreover, it was found

192 that ^{3}DMB*, $^1O_2$, and $O_2^{\bullet-}$ were the major contributors to the photosensitized oxidation of 4-ethylguaiacol (Chen et al., 2020).

193 Recently, the oxidation of guaiacyl acetone (a non-conjugated phenolic carbonyl) in the presence of DMB has been reported

194 to be initiated by ^{3}DMB*, ^{1}O$_2$, ˙OH, or methoxy radical (˙OCH$_3$) (Misovich et al., 2021). Further studies are thus required to

195 identify the specific oxidants in these reaction systems. In this study, reactions initiated in the presence of DMB or VL are

196 collectively referred to as photosensitized reactions. The reaction conditions, initial guaiacol (GUA) and DMB or VL decay

197 rate constants, normalized product abundance, and the chemical characteristics of aqSOA formed in this work are

198 summarized in Table 1.

199 3.1.1 Kinetic analysis of photosensitization by ^{3}DMB* and ^{3}VL*

200 No significant loss of GUA or photosensitizers was observed for dark experiments ($p > 0.05$). Figure S1 shows the decay of

201 GUA, DMB, and VL under different experimental conditions. Upon irradiation, the GUA decay rate constant in GUA+DMB

202 was ~4 times higher than in GUA+VL. In GUA+DMB, the decay rate constant of GUA was ~8 times higher than that of

203 DMB, consistent with a previous study (Smith et al., 2014). Contrastingly, the decay rate constant of VL was 2.4 times

204 higher than that of GUA in GUA+VL. This VL consumption was also observed in our earlier work using 0.1 mM GUA +

205 0.1 mM VL (Mabato et al., 2022). These trends could be explained by the following reasons. First, DMB has a stronger

206 photosensitizing ability than VL based on its higher quantum yield of ^{3}C* formation and longer lifetime of ^{3}DMB*

207 compared to ^{3}VL* (Felber et al., 2021). Second, VL is also a phenolic compound similar to GUA, and is therefore highly

208 reactive towards oxidation. For instance, its –OH group can be oxidized by ^{3}VL* via H-atom abstraction to form phenoxy

209 radicals which can undergo coupling to form oligomers (Kobayashi and Higashimura, 2003; Sun et al., 2010; Mabato et al.,

210 2022). The faster consumption of VL than GUA suggests a competition between ground-state VL and GUA for reaction with

211 ^{3}VL*. Moreover, compared to a –OCH$_3$ group (in DMB), an –OH group (in VL) has a stronger electron-donating ability and

212 is thus more activating towards electrophilic aromatic substitution. It should be noted that the differences in the GUA decay

213 rate constants among different reaction systems are not quantitatively equivalent to photosensitizing efficiencies, and a

214 detailed quantitative analysis of which is beyond the scope of this study. Nonetheless, these results suggested that GUA

215 oxidation in GUA+DMB was overall more efficient than in GUA+VL. Our kinetic analysis focused on the decay rate

216 constants of the aqSOA precursor (GUA) and the photosensitizers (DMB and VL) during photosensitization under the same

217 experimental conditions (same aqSOA precursor and concentration, same photosensitizer concentration, and same lamp

218 photon flux). The effects of other factors (e.g., intersystem crossing efficiency) on the rate constants were not examined.

219 Explicit kinetic studies (e.g., Smith et al., 2014, 2015) that measure second-order rate constants should be conducted in the

220 future to extend the applicability of the kinetic parameters to other conditions.

221 3.1.2 Product distributions and chemical characteristics of aqSOA from photosensitization by ^{3}DMB* and ^{3}VL*

222 The products detected using UHPLC-HESI-Orbitrap-MS were used to characterize the aqSOA formed in this work. The

223 signal-weighted distributions of aqSOA calculated from combined positive (POS) and negative (NEG) ion modes MS results

224 are summarized in Figure 2. The signal-weighted distributions calculated separately from POS and NEG ion modes MS

225 results are available in Figures S2 and S3. It should be noted that in this work, the product distributions for all experiments

were based on the same irradiation time of 180 min. An irradiation time of 180 min was chosen as it was sufficient to show the differences in the extent of reaction of GUA among the reaction systems studied. For reaction systems with precursors of different reactivities, chemical analysis at a fixed reaction time may be looking at different generations of products of each precursor, as Yu et al. (2014) reported. Measuring the product distribution at a fixed time might have missed the information on what/how many products are formed at the similar amounts of precursors reacted. The situation could be even more complicated if different precursors had major differences in pathways and dominant intermediates. However, comparing the product distributions after a certain time of light exposure, as is the case for this study, is useful to evaluate what products would form after a certain time of photosensitization. Oligomers and derivatives of GUA dominated both GUA+DMB and GUA+VL, in agreement with pronounced oligomerization from triplet-mediated oxidation of relatively high phenol concentration (e.g., 0.1 to 3 mM; Li et al., 2014; Yu et al., 2014, 2016; Slikboer et al., 2015; Ye et al., 2019; Mabato et al., 2022). Figure 3 schematically depicts the main differences between photosensitized GUA oxidation by ^{3}DMB* and ^{3}VL* in the absence and presence of AN. As shown in Fig. 3, ^{3}DMB* and ^{3}VL* can oxidize GUA via H-atom abstraction to form phenoxy radicals which undergo coupling to form oligomers (Kobayashi and Higashimura, 2003; Sun et al., 2010; Mabato et al., 2022). The higher oligomer contribution in GUA+DMB is likely due to the better photosensitizing ability of DMB than VL and partly the lower abundance of ^{3}VL* due to fast VL consumption. VL was consumed faster than DMB during GUA oxidation ascribable to the –OH group of VL, making it more susceptible to oxidation and more reactive towards electrophilic aromatic substitution. In addition, the normalized product abundance for GUA+DMB was ~4 times higher than that for GUA+VL (Table 1), further suggesting more efficient photosensitized GUA oxidation by ^{3}DMB* than by ^{3}VL*. The oxidation of GUA or transient organic intermediates by secondary oxidants (e.g., $^1O_2$ and $^\bullet$OH) from ^{3}DMB* or ^{3}VL* and the fragmentation of larger compounds generate highly oxidized ring-opening products (Yu et al., 2014; Huang et al., 2018; Chen et al., 2020). GUA+DMB had a higher contribution of ring-opening products than GUA+VL, likely due to the greater availability of secondary oxidants in the former and fast VL consumption lowering the production of these species in GUA+VL. The IC analyses also indicate the formation of small organic acids (e.g., formic acid), which appeared to have higher concentrations in the presence of DMB than in VL (Fig. S4). Although no data is available for the concentration changes (every 30 min) of small organic acids during the reaction, it is likely that an increasing trend would be observed as fragmentation, which leads to the decomposition of initially formed oligomers and the generation of smaller oxygenated products, becomes important at longer irradiation times (Huang et al., 2018). This trend has also been observed in our previous work on the direct photosensitized oxidation of VL (Mabato et al., 2022), as well as other studies on photosensitized oxidation of non-carbonyl phenols and phenolic carbonyls (e.g., Yu et al., 2016; Jiang et al., 2021). The reactions of secondary oxidants or ring-opening products with GUA can form functionalized products. Notably, the contribution of monomers in GUA+VL was almost twice as high as in GUA+DMB, ascribable to VL transformation products. We previously showed that for the direct photosensitized oxidation of VL, functionalization prevails over oligomerization at 0.01 mM VL, the [VL] used in this work, while oligomerization dominates at higher [VL] (0.1 mM; Mabato et al., 2022).

260   It has been reported that oligomerization could occur during the electrospray ionization process (Yasmeen et al.,

261   2010). In this work, it was confirmed that the oligomers observed were generated in the solutions via aqueous reactions

262   instead of being artefacts of HESI-MS. This is based on the absence of dimers and higher oligomers in the HESI mass

263   spectra of dark control solutions acquired by direct infusion (Yu et al., 2016).

264   The major GUA+DMB and GUA+VL products (Tables S1-S2) are mostly oligomers which can be formed through

265   the coupling of phenoxy radicals (Kobayashi and Higashimura, 2003; Sun et al., 2010; Mabato et al., 2022). GUA+DMB

266   products matched those reported in previous works on ^{3}DMB*- and/or $^{\bullet}$OH-mediated phenol oxidation (Yu et al., 2014,

267   2016). These include GUA dimers and trimers (e.g., $C_{14}H_{14}O_4$ and $C_{21}H_{18}O_8$, #1 and 19; Table S1), aldehydes ($C_7H_6O_4$, #13;

268   Table S1), and esters ($C_{16}H_{18}O_6$, #14; Table S1). Functionalized products include $C_{11}H_{12}O_5$ and $C_{10}H_{12}O_3$ (#8 and 12; Table

269   S1). More than half of the major GUA+VL products are the same oligomers detected from GUA+DMB (e.g., $C_{13}H_{10}O_4$ and

270    $C_{20}H_{18}O_6$, #4 and 21; Table S1). The rest are mainly functionalized species such as $C_7H_8O_4$ and $C_8H_8O_5$ (#28 and 35; Table

271   S2), corresponding to a hydroxylated GUA and hydroxylated VL, respectively.

272   The average elemental ratios and elemental distribution of the products (Fig. S5a–d) were consistent with those in

273   previous studies on similar reaction systems (Yu et al., 2014, 2016; Mabato et al., 2022). The majority of the GUA+DMB

274   and GUA+VL products had H:C $\leq$1.0 and O:C $\leq$0.5, typical for aromatic species (Mazzoleni et al., 2012; Kourtchev et al.,

275   2014; Jiang et al., 2021). GUA+DMB had more compounds with higher O:C ($\geq$0.6), in agreement with higher contributions

276   of ring-opening products than in GUA+VL (Fig. 2). The higher $\langle OS_C \rangle$ for GUA+VL than in GUA+DMB (Table 1) was

277   probably due to the significant functionalization in the former. Moreover, the distributions of OS_C and carbon number (Fig.

278   S6a–d) show that these aqSOA products have similar elemental composition to those of low-volatility oxygenated organic

279   aerosols (LV-OOA), semi-volatile oxygenated organic aerosols (SV-OOA), and slightly with biomass burning organic

280   aerosols (BBOA) (Kroll et al., 2011). Further discussions on van Krevelen diagrams (Fig. S5a–d) and OS_C vs. carbon

281   number plots (Fig. S6a–d) for GUA+DMB and GUA+VL aqSOA are available in the Supplement (Sect. S5). In brief,

282   ^{3}DMB*-initiated GUA oxidation was faster and yielded higher normalized product abundance than oxidation by ^{3}VL*. This

283   is likely due to the stronger photosensitizing ability of DMB than VL and the –OH group of VL facilitating its rapid

284   consumption. In addition, oligomerization and functionalization dominated in both GUA+DMB and GUA+VL, as reported

285   in similar studies (Yu et al., 2014, 2016; Chen et al., 2020; Jiang et al., 2021; Misovich et al., 2021; Mabato et al., 2022).

286   However, functionalization was more prominent in the latter, attributable to the transformation of VL. Nonetheless, it must

287   be noted that for phenolic aqSOA, fragmentation will ultimately be more predominant at longer irradiation times (Huang et

288   al., 2018; Yu et al., 2016; Mabato et al., 2022).

289   **3.1.3 Light absorption of aqSOA from photosensitization by ^{3}DMB* and ^{3}VL***

290   The absorbance enhancement of phenolic aqSOA generated via reactions with ^{3}C~~DMB*/^{3}VL*~~ has been linked to the

291   formation of conjugated structures due to oligomerization and functionalization (e.g., additions of hydroxyl and carbonyl

292   groups; Yu et al., 2014, 2016; Smith et al., 2016; Ye et al., 2019; Chen et al., 2020; Jiang et al., 2021; Misovich et al., 2021;

Ou et al., 2021; F. Li et al., 2022; X. Li et al., 2022; Mabato et al., 2022; Wang et al., 2022). Moreover, the aqueous-phase photo-oxidation of BB emissions can enhance BrC absorbance via the formation of aromatic dimers and functionalized products (Hems et al., 2020). The increase in light absorption throughout 180 min of irradiation and the change in the rate of sunlight absorption (ΔR_{abs}) (Jiang et al., 2021) from 350 to 550 nm at 180 min during typical clear and haze days in Beijing, China for all the reaction systems studied are provided in Figure 4. Figure S7 shows the absorption spectra after 180 min of irradiation for each reaction system studied. In this work, the absorbance enhancement of GUA+DMB and GUA+VL (Fig. 4a) could be due to oligomers and functionalized monomers, which are the highest contributors to the product signals. Identifying the chromophores responsible for the absorbance enhancement may be beneficial in understanding the impact of aqSOA on the Earth's radiative balance and determining the reactions that affect light absorption by aqSOA (Mabato et al., 2022). However, the detected products did not exhibit distinct peaks in the UHPLC-PDA chromatograms, likely due to the concentration of the chromophores being below the detection limit of PDA. Nevertheless, the higher absorbance enhancement and ΔR_{abs} for GUA+DMB than GUA+VL was probably due to the higher contribution and normalized abundance (by ~6 times) of oligomers in the former.

Additional information about aqSOA lightabsorption can be deduced from the plots of the double bond equivalent (DBE) values vs. carbon number (n_C) (Lin et al., 2018). Figure S8 shows these plots along with the DBE reference values of fullerene-like hydrocarbons (Lobodin et al., 2012), cata-condensed polycyclic aromatic hydrocarbons (PAHs; Siegmann and Sattler, 2000), and linear conjugated polyenes with a general formula C_xH_{x+2}. The shaded area indicates a sufficient level of conjugation for visible light absorption, and species within this region are potential BrC chromophores. GUA+DMB and GUA+VL aqSOA exhibited a significant overlap in the DBE vs. n_C space; nearly all products from both systems, including the high-relative-abundance species, are potential BrC chromophores. GUA+DMB had more oligomeric products with high relative abundance ($n_C \geq 12$ and DBE ≥ 8). For GUA+VL, high-relative-abundance products also include monomeric species ($n_C = 7-8$ and 4-5 DBE) corresponding to hydroxylated products (e.g., $C_7H_8O_4$ and $C_8H_8O_5$; 28 and 35; Table S2). These observations further indicate the importance of oligomerization and functionalization for the absorbance enhancement of aqSOA generated via photosensitization by $^3DMB^*$ and $^3VL^*$. In summary, $^3DMB^*$ and $^3VL^*$ can oxidize GUA resulting in aqSOA and BrC formation, but GUA+DMB products exhibited stronger light absorption. In GUA+VL, the extent of GUA oxidation was limited by significant VL consumption.

3.2 Comparison of photosensitized GUA oxidation by non-phenolic ($^3DMB^*$) and phenolic ($^3VL^*$) methoxybenzaldehydes in the presence of AN

3.2.1 Kinetic analysis of photosensitization by $^3DMB^*$ and $^3VL^*$ in the presence of AN

Ammonium nitrate (AN) did not significantly affect ($p > 0.05$) the decay rate constants of GUA, DMB, and VL for both GUA+DMB+AN and GUA+VL+AN (Table 1), likely due to the higher molar absorptivities of the photosensitizers compared to that of nitrate. This implies that the chemistry of $^3DMB^*$ and $^3VL^*$ dominated that of nitrate. In this work, the GUA decay rate constants decreased in the order of GUA+DMB/GUA+DMB+AN > GUA+VL/GUA+VL+AN > GUA+AN

(Table 1). Note that as the molar absorptivities of the photosensitizers are higher than that of nitrate, the kinetics data were also analyzed on a per-photon-absorbed basis for a more appropriate comparison of reaction efficiency (Sect. S6). The apparent quantum efficiency of GUA photodegradation (φ_{GUA}) in the presence of nitrate (GUA+AN: $0.17 \pm 3.8 \times 10^{-2}$) was ~2 and ~7 times higher than that in the presence of DMB ($0.10 \pm 2.9 \times 10^{-3}$) or VL ($0.026 \pm 7.2 \times 10^{-3}$), respectively. This suggests that nitrate-mediated GUA photo-oxidation is more efficient than photosensitization by ^{3}DMB* or ^{3}VL* on a per-photon-absorbed basis.

3.2.2 Product distributions and chemical characteristics of aqSOA from photosensitization by ^{3}DMB* and ^{3}VL* in the presence of AN

For both GUA+DMB+AN and GUA+VL+AN, AN had no significant effect on the normalized product abundance (Table 1), but it induced the formation of N-containing products composed of N-heterocycles (e.g., imidazoles and pyridines) and oligomers, as well as nitrated species. Similarly, we previously reported a potential imidazole derivative from the direct photosensitized oxidation of VL in the presence of AN, which was attributed to the reaction of ring-opening products with dissolved ammonia (Mabato et al., 2022). Oligomers remained the highest signal contributors in the presence of AN (Fig. 2), but interactions between photosensitization by ^{3}DMB* and ^{3}VL* and AN photolysis were distinct. First, nitrated species had similar contributions in both cases, but the contribution and normalized abundance of all N-containing products in GUA+DMB+AN were 2 and ~14 times higher, respectively, than in GUA+VL+AN. This difference can be attributed to the higher contribution of N-heterocycles and N-containing oligomers in GUA+DMB+AN. Compared to GUA+VL, GUA+DMB had a higher contribution of ring-opening products which can react with ammonia, as discussed earlier (Figs. 2 and 3). Second, the decrease in oligomers in GUA+DMB+AN may be due to their fragmentation induced by ·OH from nitrate photolysis, then conversion to N-containing products. Correspondingly, the contribution of possibly ring-retaining N-containing products in GUA+DMB+AN (18.6%) was ~3 times higher than that in GUA+VL+AN (6.5%). While fragmentation of oligomers likely occurred in GUA+VL+AN as well, the increase in oligomers suggests that other reactions have taken place. For GUA+VL+AN, ·OH or ·NO$_2$ from nitrate photolysis may have initiated H-atom abstraction from the –OH group of VL, generating phenoxy radicals which can undergo coupling to form more oligomers (Kobayashi and Higashimura, 2003; Sun et al., 2010; Mabato et al., 2022). This may also explain the more significant decrease of monomers in GUA+VL+AN (~3 times) compared to GUA+DMB+AN (~2 times). Similarly, we previously observed an increase in oligomers during the direct photosensitized oxidation of 0.01 mM VL (Mabato et al., 2022), the [VL] used in this work, upon adding 1 mM AN. These findings indicate that photosensitization by non-phenolic and phenolic methoxybenzaldehydes may interact differently with AN photolysis.

GUA+AN mainly formed oligomers analogous to ·OH-mediated phenol oxidation (Yu et al., 2014, 2016), followed by N-containing products. The normalized product abundance of GUA+AN was the lowest among all experiments, likely due to the lower GUA decay constant relative to photosensitized oxidation. Moreover, the normalized abundance of N-containing products in GUA+AN was ~12 times lower than that in GUA+DMB+AN but comparable to that in

359 GUA+VL+AN. This discrepancy for GUA+VL+AN might be due to the weaker signals of its N-containing products in the

360 positive compared to the negative ion mode. As previously mentioned, the normalized product abundance was calculated

361 using only the positive ion mode data as the GUA signal from the negative ion mode was weak and thus may present large

362 uncertainties during normalization. Interestingly, the contributions from nitrated species in GUA+DMB+AN and

363 GUA+VL+AN were higher than in GUA+AN, suggesting possible enhancement of nitration reactions. This is likely due to

364 the increased formation of $^\bullet NO_2$, for instance, via the reactions of $^\bullet OH$ and $O_2^{\bullet-}$ (from $^3DMB^*$ or $^3VL^*$) with NO_2^- (Pang et

365 al., 2019; Mabato et al., 2022). Similarly, we previously reported enhanced nitration via the direct photosensitized oxidation

366 of VL in the presence of AN under air-saturated conditions (O_2 is present) relative to nitrogen-saturated conditions (Mabato

367 et al., 2022). These imply that photosensitization may promote reactions induced by nitrate photolysis.

368   The major products from GUA+DMB+AN, GUA+VL+AN, and GUA+AN (Tables S3–S5) include oligomers and

369 functionalized monomers detected in GUA+DMB and GUA+VL (Tables S1–S2). The N-heterocycles from

370 GUA+DMB+AN include $C_6H_6N_4$ (#41; Table S3), which may be 2,2'-biimidazole (BI), a reaction product from glyoxal +

371 reduced nitrogenous compounds (e.g., ammonium salts) (De Haan et al., 2009; Galloway et al., 2009; Nozière et al., 2009;

372 Shapiro et al., 2009; Yu et al., 2011; Kampf et al., 2012; Gen et al., 2018; Mabato et al., 2019). The nitrated products include

373 $C_{12}H_{11}N_3O_3$ and $C_{15}H_{10}N_4O_3$ (#42 and 49; Table S3), which possibly have a nitrated imidazole moiety and a nitrophenol

374 moiety, respectively. For GUA+VL+AN, oligomers ($C_{14}H_{12}O_6$ and $C_{20}H_{16}O_7$; #55 and 59, Table S4) which were not among

375 the major products in GUA+VL were noted. $C_{10}H_8O_2$ likely has a furanone group (#50; Table S4); furanones are the primary

376 products of the reaction of $^\bullet OH$ with toluene and other aromatic hydrocarbons (Smith et al., 1999). Moreover, $C_{11}H_9N_3O_3$

377 (#57; Table S4) has a nitrated imidazole moiety. Among the N-containing compounds in GUA+AN is $C_4H_3N_3O_3$ (#69; Table

378 S5), which may be a nitrated imidazole-2-carboxaldehyde. Imidazole-2-carboxaldehyde is also a reaction product from

379 glyoxal + reduced nitrogenous compounds (e.g., ammonium salts) (De Haan et al., 2009; Galloway et al., 2009; Nozière et

380 al., 2009; Shapiro et al., 2009; Yu et al., 2011; Kampf et al., 2012; Gen et al., 2018; Mabato et al., 2019).

381   The ⟨O:C⟩ for GUA+DMB+AN and GUA+VL+AN were lower than those in the absence of AN (Table 1), possibly

382 due to the formation of N-heterocycles, altering the elemental ratios. The ⟨O:C⟩ and ⟨H:C⟩ were comparable in

383 GUA+DMB+AN and GUA+VL+AN, but the ⟨N:C⟩ for the former was higher, implying a greater extent of reactions

384 involving AN. Relative to GUA+DMB+AN and GUA+VL+AN, GUA+AN had a higher ⟨N:C⟩, as can be expected given

385 that AN was the only oxidant source. The lower ⟨OS_C⟩ of GUA+DMB+AN and GUA+VL+AN compared to GUA+AN may

386 be attributed to triplet-initiated oxidation generating higher-molecular-weight products with less fragmentation compared to

387 $^\bullet OH$-mediated oxidation (Yu et al., 2014; Chen et al., 2020). Nonetheless, AN generally increased the ⟨OS_C⟩ for both

388 GUA+DMB and GUA+VL, with a more noticeable increase for the former, suggesting more oxidized products. Similarly, in

389 a previous work, the more oxygenated and oxidized aqSOA from the photo-oxidation of phenolic carbonyls in AN solutions

390 than in ammonium sulfate solutions has been ascribed to nitrate photolytic products promoting the reactions (Huang et al.,

391 2018). Furthermore, GUA+DMB+AN and GUA+VL+AN aqSOA had mainly similar features in the OS_C vs. n_C plots as

392 those observed in the absence of AN (Fig. S6). More information on van Krevelen diagrams (Figs. S5e–h and S9) and OS_C

393 vs. n_C plots (Figs. S6e–h and S10) for GUA+DMB+AN, GUA+VL+AN, and GUA+AN aqSOA are provided in the

394 Supplement (Sect. S7). In essence, AN had no significant effect on the decay kinetics ascribable to photosensitizer chemistry

395 prevailing over nitrate, but it induced the formation of N-containing products. Moreover, AN modified the product

396 distributions, albeit in different ways (Figs. 2 and 3). In particular, N-containing products were more abundant in

397 GUA+DMB+AN, probably due to more extensive fragmentation in GUA+DMB than in GUA+VL. In GUA+VL+AN, AN

398 promoted oligomer formation likely via the -OH group of VL. Furthermore, GUA+DMB+AN and GUA+VL+AN had more

399 nitrated products than GUA+AN, suggesting that photosensitized reactions may promote nitrate photolysis-initiated

400 reactions.

401 **3.2.3 Light absorption of aqSOA from photosensitization by [3]DMB* and [3]VL* in the presence of AN**

402 The presence of AN also did not appreciably affect the absorbance enhancement and ΔR_{abs} for both GUA+DMB+AN and

403 GUA+VL+AN (Fig. 4). For GUA+DMB+AN, the N-containing products may have offset the decrease in oligomers to

404 maintain the absorbance enhancement observed from GUA+DMB. Wang et al. (2022) reported that nitration might

405 contribute significantly to absorbance enhancement for methoxyphenols in sodium nitrate. In GUA+VL+AN, the decrease in

406 monomers may have counteracted the increased oligomers and the generated N-containing products. Compared to

407 GUA+DMB+AN, the N-containing products from GUA+VL+AN probably had less impact on the absorbance enhancement

408 based on their smaller signal contribution.

409 Similar to experiments without AN, CHO species from GUA+DMB+AN and GUA+VL+AN were mainly

410 overlapped in the DBE vs. n_C space (Fig. S8c,d) and were mostly potential BrC chromophores. In both systems, GUA dimers

411 were the products with the highest relative abundance. For GUA+DMB+AN, products with high relative abundance also

412 include a CHN species, while two CHON species had high n_C (18,20) and DBE (16,14) values. In GUA+VL+AN, products

413 with high relative abundance include a CHON species (n_C = 11 and 9 DBE). Approximately 30% and 43% of the N-

414 containing products for GUA+DMB+AN and GUA+VL+AN, respectively, were among the potential BrC chromophores.

415 This suggests the possible significance of N-containing products for light absorption of aqSOA from photosensitization by

416 methoxybenzaldehydes and AN photolysis. Correspondingly, nitroaromatic compounds and N-heterocycles are frequently

417 noted in BBOA (Iinuma et al., 2010; Kitanovski et al., 2012; Kourtchev et al., 2016) and have been proposed to be potential

418 contributors to BrC light absorption (Laskin et al., 2015). Relative to GUA+DMB+AN and GUA+VL+AN, only 19% of the

419 N-containing products in GUA+AN were potential BrC chromophores (Fig. S8e,f), and these did not include CHN species.

420 These indicate that the N-containing products formed in the presence of both photosensitizers and AN may be more

421 significant contributors to the light absorption of phenolic aqSOA than those formed in AN only.

4 Conclusions and atmospheric implications

The photosensitized oxidation of guaiacol (GUA) by triplet excited states of 3,4-dimethoxybenzaldehyde (^{3}DMB*) and vanillin (^{3}VL*) (separately) in the absence and presence of ammonium nitrate (AN) were compared under identical conditions (simulated sunlight and concentration) relevant to atmospheric cloud and fog waters. Compared to GUA+VL, faster GUA oxidation and stronger light absorption by the products were observed in GUA+DMB. Moreover, VL was consumed faster relative to DMB, limiting the extent of GUA oxidation in GUA+VL. These differences are rooted in DMB having a better photosensitizing ability than VL and the –OH group of VL, making it more susceptible to oxidation and more reactive towards electrophilic aromatic substitution. Both GUA+DMB and GUA+VL generated aqSOA (including potential BrC chromophores) composed of oligomers, functionalized monomers, oxygenated ring-opening products, and N-containing products in the presence of AN. The major aqSOA formation processes for GUA+DMB and GUA+VL were oligomerization and functionalization, but functionalization appeared to be more significant in GUA+VL due to VL transformation products. The photochemical evolution of aqSOA from GUA+DMB has been reported by Yu et al. (2016). Similar experiments for aqSOA from GUA+VL should be conducted in the future to better understand photosensitized reactions involving phenolic carbonyl photosensitizers.

AN did not significantly affect the decay kinetics due to the predominant effect of ^{3}DMB* and ^{3}VL* chemistry compared to nitrate, but it promoted the formation of N-containing products; these are composed of N-heterocycles (e.g., imidazoles) and oligomers and nitrated species. The observation of N-heterocycles agrees with our previous findings that ammonium participates in photosensitized oxidation of phenolic compounds in the presence of AN (Mabato et al., 2022). These results also suggest that photosensitized oxidation of phenolic compounds in the presence of AN might be an important source of N-heterocycles and nitrated products. Identifying the sources of N-heterocycles and nitrated compounds is important due to their environmental and health impacts (Laskin et al., 2009). Moreover, photosensitized reactions by non-phenolic and phenolic methoxybenzaldehydes may be differently influenced by AN photolysis. For instance, the more extensive fragmentation in GUA+DMB than in GUA+VL possibly resulted in more N-containing products in GUA+DMB+AN. Furthermore, the increased oligomers in GUA+VL+AN may be due to VL-derived phenoxy radicals induced by $^•$OH or $^•$NO$_2$ from nitrate photolysis. In addition, more nitrated compounds observed in GUA+DMB+AN and GUA+VL+AN than in GUA+AN imply that photosensitized reactions may promote nitrate-mediated photolytic reactions. On a related note, the significance of photosensitization by BrC (via formation of solvated electrons; Y. Wang et al., 2021) and marine dissolved organic matter (via O$_2$$^{•-}$ formation; Garcia et al., 2021) in enhanced nitrite production from nitrate photolysis have been reported. A recent study from our group has shown that glyoxal photo-oxidation mediated by both nitrate photolysis and photosensitization can significantly enhance the atmospheric sink of glyoxal (Zhang et al., 2022). Further studies are needed to improve our understanding of the interplay between photosensitized reactions and nitrate photolysis.

454   This study demonstrates that the structural features of photosensitizers affect aqSOA formation via non-carbonyl

455   phenol oxidation. The VL results are broadly relevant to other phenolic carbonyls, but the effects of different functional

456   groups should still be considered. For instance, the aldehyde/ketone pair of syringaldehyde and acetosyringone, both

457   phenolic carbonyls, have been reported to have equal reactivity towards direct photosensitized oxidation. This is due to the

458   greater light absorption by the aldehyde form but higher quantum efficiency for loss for the ketone form (Smith et al. 2016).

459   However, more aqSOA was observed from syringaldehyde than acetosyringone (in either AN or ammonium sulfate; Huang

460   et al., 2018). Our findings also imply that while the contributions of photosensitization by ^{3}VL* (and other phenolic

461   carbonyls) to aqSOA formation would be relatively less compared to that of ^{3}DMB* (and other non-phenolic carbonyls),

462   these are not negligible. As both non-phenolic and phenolic carbonyls such as the methoxybenzaldehydes examined in this

463   work are emitted in large amounts from biomass burning, future experiments should probe the aqSOA contribution of a

464   wider variety of photosensitizers. Moreover, further experiments on photosensitized reactions in authentic particulate matter

465   (PM) samples should be conducted in the future. Multicomponent reactions such as GUA+DMB+AN and GUA+VL+AN

466   should also be explored for a more accurate simulation of ambient conditions. These would be useful in assessing the overall

467   impact of photosensitized reactions and AN photolysis on aqSOA formation in areas impacted by biomass burning and high

468   AN concentrations, and for their better representation in aqSOA models.

469

470   *Data availability.*

471   The data used in this publication are available to the community and can be accessed by request to the corresponding author.

472   *Author contributions.*

473   BRGM designed and conducted the experiments; BRGM and CKC wrote the paper. All co-authors contributed to the

474   discussion of the manuscript.

475   *Competing interests.*

476   The authors declare that they have no conflict of interest.

477   *Acknowledgments.*

478   C.K.C. gratefully acknowledges support from the National Natural Science Foundation of China (42075100, 41875142, and

479   42275104) and Hong Kong Research Grants Council (11304121). Y.J.L. acknowledges funding support from the Science

480   and Technology Development Fund, Macau SAR (File No. 0019/2020/A1), and a multiyear research grant (No.

481   MYRG2018-00006-FST) from the University of Macau. The authors also thank the University Research Facility in

482   Chemical and Environmental Analysis (UCEA) at The Hong Kong Polytechnic University for the use of its UHPLC-HESI-

483   Orbitrap Mass Spectrometer and Dr Sirius Tse and Dr Chi Hang Chow for assistance with sample analyses.

References

Anastasio, C., Faust, B. C., and Rao, C. J.: Aromatic carbonyl compounds as aqueous-phase photochemical sources of hydrogen peroxide in acidic sulfate aerosols, fogs, and clouds. 1. Non-phenolic methoxybenzaldehydes and methoxyacetophenones with reductants (phenols), Environ. Sci. Technol., 31, 218−232, https://doi.org/10.1021/es960359g, 1997.

Aregahegn, K. Z., Felber, T., Tilgner, A., Hoffmann, E. H., Schaefer, T., and Herrmann, H.: Kinetics and mechanisms of aqueous-phase reactions of triplet-state imidazole-2-carboxaldehyde and 3,4-dimethoxybenzaldehyde with α,β-unsaturated carbonyl compounds, J. Phys. Chem. A, 126, 8727–8740, https://doi.org/10.1021/acs.jpca.2c05015, 2022.

Bateman, A. P., Laskin, J., Laskin, A., and Nizkorodov, S. A.: Applications of high-resolution electrospray ionization mass spectrometry to measurements of average oxygen to carbon ratios in secondary organic aerosols, Environ. Sci. Technol., 46, 8315–832, https://doi.org/10.1021/es3017254, 2012.

Bianco, A., Passananti, M., Brigante, M., and Mailhot, G.: Photochemistry of the cloud aqueous phase: a review, Molecules, 25, 423, https://doi.org/10.3390/molecules25020423, 2020.

Calvert, J. G. and Madronich, S.: Theoretical study of the initial products of the atmospheric oxidation of hydrocarbons, J. Geophys. Res., 92, 2211−2220, https://doi.org/10.1029/JD092iD02p02211, 1987.

Chen, H., Ge, X., and Ye, Z.: Aqueous-phase secondary organic aerosol formation via reactions with organic triplet excited states – a short review, Curr. Pollut. Rep., 4, 8–12, https://doi.org/10.1007/s40726-018-0079-7, 2018.

Chen, Y., Li, N., Li, X., Tao, Y., Luo, S., Zhao, Z., Ma, S., Huang, H., Chen, Y., Ye, Z., and Ge, X.: Secondary organic aerosol formation from $^3C^*$-initiated oxidation of 4-ethylguaiacol in atmospheric aqueous-phase, Sci. Total Environ., 723, 137953, https://doi.org/10.1016/j.scitotenv.2020.137953, 2020.

Chen, Z. and Anastasio, C.: Concentrations of a triplet excited state are enhanced in illuminated ice, Environ. Sci.: Processes Impacts, 19, 12−21, https://doi.org/10.1039/C6EM00534A, 2017.

Collett, J. L. Jr., Hoag, K. J., Sherman, D. E., Bator, A., and Richards, L. W.: Spatial and temporal variations in San Joaquin Valley fog chemistry, Atmos. Environ., 33, 129−140, https://doi.org/10.1016/S1352-2310(98)00136-8, 1998.

De Haan, D. O., Tolbert, M. A., and Jimenez, J. L.: Atmospheric condensed-phase reactions of glyoxal with methylamine, Geophys. Res. Lett., 36, No. L11819, https://doi.org/10.1029/2009GL037441, 2009.

De Haan, D. O., Hawkins, L. N., Kononenko, J. A., Turley, J. J., Corrigan, A. L., Tolbert, M. A., and Jimenez, J. L.: Formation of nitrogen-containing oligomers by methylglyoxal and amines in simulated evaporating cloud droplets, Environ. Sci. Technol., 45, 984−991, https://doi.org/10.1021/es102933x, 2011.

De Haan, D. O., Pajunoja, A., Hawkins, L. N., Welsh, H. G., Jimenez, N. G., De Loera, A., Zauscher, M., Andretta, A. D., Joyce, B. W., De Haan, A. C., Riva, M., Cui, T., Surratt, J. D., Cazaunau, M., Formenti, P., Gratien, A., Pangui, E., and Doussin, J-F.: Methylamine's effects on methylglyoxal-containing aerosol: chemical, physical, and optical changes, ACS Earth Space Chem., 3, 1706–1716, https://doi.org/10.1021/acsearthspacechem.9b00103, 2019.

Du, Y., Fu, Q. S., Li, Y., and Su, Y.: Photodecomposition of 4-chlorophenol by reactive oxygen species in UV/air system, J. Hazard. Mater., 186, 491–496, https://doi.org/10.1016/j.jhazmat.2010.11.023, 2011.

Edye, L. A. and Richards, G. N.: Analysis of condensates from wood smoke. components derived from polysaccharides and lignins, Environ. Sci. Technol., 25, 1133−1137, https://doi.org/10.1021/es00018a018, 1991.

Felber, T., Schaefer, T., He, L., and Herrmann, H.: Aromatic carbonyl and nitro compounds as photosensitizers and their photophysical properties in the tropospheric aqueous phase, J. Phys. Chem. A, 125, 5078−5095, https://doi.org/10.1021/acs.jpca.1c03503, 2021.

Fleming, L. T., Lin, P., Laskin, A., Laskin, J., Weltman, R., Edwards, R. D., Arora, N. K., Yadav, A., Meinardi, S., Blake, D. R., Pillarisetti, A., Smith, K. R., and Nizkorodov, S. A.: Molecular composition of particulate matter emissions from dung and brushwood burning household cookstoves in Haryana, India, Atmos. Chem. Phys., 18, 2461–2480, https://doi.org/10.5194/acp-18-2461-2018, 2018.

Galloway, M. M., Chhabra, P. S., Chan, A. W. H., Surratt, J. D., Flagan, R. C., Seinfeld, J. H., and Keutsch, F. N.: Glyoxal uptake on ammonium sulphate seed aerosol: reaction products and reversibility of uptake under dark and irradiated conditions, Atmos. Chem. Phys., 9, 3331–3345, https://doi.org/10.5194/acp-9-3331-2009, 2009.

Garcia, S. L. M., Pandit, S., Navea, J. G., and Grassian, V. H.: Nitrous acid (HONO) formation from the irradiation of aqueous nitrate solutions in the presence of marine chromophoric dissolved organic matter: comparison to other organic photosensitizers, ACS Earth Space Chem., 5, 3056−3064, https://doi.org/10.1021/acsearthspacechem.1c00292, 2021.

Gen, M., Huang, D. D., and Chan, C. K.: Reactive uptake of glyoxal by ammonium-containing salt particles as a function of relative humidity, Environ. Sci. Technol., 52, 6903−6911, https://doi.org/10.1021/acs.est.8b00606, 2018.

Gen, M., Zhang, R., Huang, D. D., Li, Y. J., and Chan, C. K.: Heterogeneous SO_2 oxidation in sulfate formation by photolysis of particulate nitrate, Environ. Sci. Technol. Lett., 6, 86–91, https://doi.org/10.1021/acs.estlett.8b00681, 2019a.

Gen, M., Zhang, R., Huang, D. D., Li, Y. J., and Chan, C. K.: Heterogeneous oxidation of SO_2 in sulfate production during nitrate photolysis at 300 nm: effect of pH, relative humidity, irradiation intensity, and the presence of organic compounds, Environ. Sci. Technol., 53, 8757–8766, https://doi.org/10.1021/acs.est.9b01623, 2019b.

Gen, M., Liang, Z., Zhang, R., Mabato, B. R. G., and Chan, C. K.: Particulate nitrate photolysis in the atmosphere, Environ. Sci.: Atmos., 2, 111–127, https://doi.org/10.1039/d1ea00087j, 2022.

George, C., Brüggemann, M., Hayeck, N., Tinel, L., and Donaldson, J.: Interfacial photochemistry: physical chemistry of gas-liquid interfaces, in: Developments in Physical & Theoretical Chemistry, edited by: Faust, J. A. and House, J. E., Elsevier, 435–457, https://doi.org/10.1016/B978-0-12-813641-6.00014-5, 2018.

Giulianelli, L., Gilardoni, S., Tarozzi, L., Rinaldi, M., Decesari, S., Carbone, C., Facchini, M. C., and Fuzzi, S.: Fog occurrence and chemical composition in the Po valley over the last twenty years, Atmos. Environ., 98, 394–401, https://doi.org/10.1016/j.atmosenv.2014.08.080, 2014.

Grace, D. N., Sharp, J. R., Holappa, R. E., Lugos, E. N., Sebold, M. B., Griffith, D. R., Hendrickson, H. P., and, Galloway, M. M.: Heterocyclic product formation in aqueous brown carbon systems, ACS Earth Space Chem., 3, 2472−2481, https://doi.org/10.1021/acsearthspacechem.9b00235, 2019.

Hawthorne, S. B., Miller, D. J., Langenfeld, J. J., and Krieger, M. S.: PM-10 High-volume collection and quantitation of semi- and nonvolatile phenols, methoxylated phenols, alkanes, and polycyclic aromatic hydrocarbons from winter urban air and their relationship to wood smoke emissions, Environ. Sci. Technol., 26, 2251−2262, https://doi.org/10.1021/es00035a026, 1992.

Hems, R. F., Schnitzler, E. G., Bastawrous, M., Soong, R., Simpson, A. J., and Abbatt, J. P. D.: Aqueous photoreactions of wood smoke brown carbon, ACS Earth Space Chem., 4, 1149−1160, https://doi.org/10.1021/acsearthspacechem.0c0011, 2020.

Hoshino, M., Akimoto, H., and Okuda, M.: Photochemical oxidation of benzene, toluene, and ethylbenzene initiated by OH radicals in the gas phase, Bull. Chem. Soc. Jpn., 51, 718−724, https://doi.org/10.1246/bcsj.51.718, 1978.

Huang, D. D., Zhang, Q., Cheung, H. H. Y., Yu, L., Zhou, S., Anastasio, C., Smith, J. D., and Chan, C. K.: Formation and evolution of aqSOA from aqueous-phase reactions of phenolic carbonyls: comparison between ammonium sulfate and ammonium nitrate solutions, Environ. Sci. Technol., 52, 9215–9224, https://doi.org/10.1021/acs.est.8b03441, 2018.

Iinuma, Y., Böge, O., Gräfe, R., and Herrmann, H.: Methyl-nitrocatechols: atmospheric tracer compounds for biomass burning secondary organic aerosols, Environ. Sci. Technol., 44, 8453–8459, https://doi.org/10.1021/es102938a, 2010.

Jiang, W., Misovich, M. V., Hettiyadura, A. P. S., Laskin, A., McFall, A. S., Anastasio, C., and Zhang, Q.: Photosensitized reactions of a phenolic carbonyl from wood combustion in the aqueous phase—chemical evolution and light absorption properties of aqSOA, Environ. Sci. Technol., 55, 5199−5211, https://doi.org/10.1021/acs.est.0c07581, 2021.

Kampf, C. J., Jakob, R., and Hoffmann, T.: Identification and characterization of aging products in the glyoxal/ammonium sulfate system – implications for light-absorbing material in atmospheric aerosols, Atmos. Chem. Phys., 12, 6323–6333, https://doi.org/10.5194/acp-12-6323-2012, 2012.

Kebarle, P. A.: A brief overview of the mechanisms involved in electrospray mass spectrometry, J. Mass Spectrom., 35, 804−817, https://doi.org/10.1002/9783527628728.ch1, 2000.

Kitanovski, Z., Grgić, I., Vermeylen, R., Claeys, M., and Maenhaut, W.: Liquid chromatography tandem mass spectrometry method for characterization of monoaromatic nitro-compounds in atmospheric particulate matter, J. Chromatogr. A, 1268, 35–43, https://doi.org/10.1016/j.chroma.2012.10.021, 2012.

Klodt, A.L., Romonosky, D.E., Lin, P., Laskin, J., Laskin, A., and Nizkorodov, S.A.: Aqueous photochemistry of secondary organic aerosol of α-pinene and α-humulene in the presence of hydrogen peroxide or inorganic salts, ACS Earth Space Chem., 3, 12, 2736–2746, https://doi.org/10.1021/acsearthspacechem.9b00222, 2019.

Kobayashi, S. and Higashimura, H.: Oxidative polymerization of phenols revisited, Prog. Polym. Sci., 28, 1015–1048, https://doi.org/10.1016/S0079-6700(03)00014-5, 2003.

Kourtchev, I., Fuller, S. J., Giorio, C., Healy, R. M., Wilson, E., O'Connor, I., Wenger, J. C., McLeod, M., Aalto, J., Ruuskanen, T. M., Maenhaut, W., Jones, R., Venables, D. S., Sodeau, J. R., Kulmala, M., and Kalberer, M.: Molecular composition of biogenic secondary organic aerosols using ultrahigh-resolution mass spectrometry: comparing laboratory and field studies, Atmos. Chem. Phys., 14, 2155−2167, https://doi.org/10.5194/acp-14-2155-2014, 2014.

Kourtchev, I., Godoi, R. H. M., Connors, S., Levine, J. G., Archibald, A. T., Godoi, A. F. L., Paralovo, S. L., Barbosa, C. G. G., Souza, R. A. F., Manzi, A. O., Seco, R., Sjostedt, S., Park, J., Guenther, A., Kim, S., Smith, J., Martin, S. T., and Kalberer, M.: Molecular composition of organic aerosols in central Amazonia: an ultra-high-resolution mass spectrometry study, Atmos. Chem. Phys., 16, 11899–11913, https://doi.org/10.5194/acp-16-11899-2016, 2016.

Kroll, J. H., Donahue, N. M., Jimenez, J. L., Kessler, S. H., Canagaratna, M. R., Wilson, K. R., Altieri, K. E., Mazzoleni, L. R., Wozniak, A. S., Bluhm, H., Mysak, E. R., Smith, J. D., Kolb, C. E., and Worsnop, D. R.: Carbon oxidation state as a metric for describing the chemistry of atmospheric organic aerosol, Nat. Chem., 3, 133–139, https://doi.org/10.1038/nchem.948, 2011.

632

633 Kruve, A., Kaupmees, K., Liigand, J., and Leito, I.: Negative electrospray ionization via deprotonation: predicting the
634 ionization efficiency, Anal. Chem., 86, 4822–4830, https://doi.org/10.1021/ac404066v, 2014.

635

636 Laskin, A., Smith, J. S., and Laskin, J.: Molecular characterization of nitrogen-containing organic compounds in biomass
637 burning aerosols using high-resolution mass spectrometry, Environ. Sci. Technol., 43, 3764–3771,
638 https://doi.org/10.1021/es803456n, 2009.

639

640 Laskin, A., Laskin, J., and Nizkorodov, S. A.: Chemistry of atmospheric brown carbon, Chem. Rev., 115, 4335–4382,
641 https://doi.org/10.1021/cr5006167, 2015.

642

643 Laskin, J., Laskin, A., Nizkorodov, S. A., Roach, P., Eckert, P., Gilles, M. K., Wang, B., Lee, H. J., and Hu, Q.: Molecular
644 selectivity of brown carbon chromophores, Environ. Sci. Technol., 48, 12047–12055, https://doi.org/10.1021/es503432r,
645 2014.

646

647 Lee, A. K. Y., Zhao, R., Li, R., Liggio, J., Li, S., and Abbatt, J. P. D.: Formation of light absorbing organo-nitrogen species
648 from evaporation of droplets containing glyoxal and ammonium sulfate, Environ. Sci. Technol., 47, 12819−12826,
649 https://doi.org/10.1021/es402687w, 2013.

650

651 Lee, H. J., Aiona, P. K., Laskin, A., Laskin, J., and Nizkorodov, S. A.: Effect of solar radiation on the optical properties and
652 molecular composition of laboratory proxies of atmospheric brown carbon, Environ. Sci. Technol., 48, 10217–10226,
653 https://doi.org/10.1021/es502515r, 2014.

654

655 Leifer, A.: The Kinetics of environmental aquatic photochemistry: Theory and practice, American Chemical Society,
656 Washington, DC, 1988.

657

658 Leito, I., Herodes, K., Huopolainen, M., Virro, K., Künnapas, A., Kruve, A., and Tanner, R.: Towards the electrospray
659 ionization mass spectrometry ionization efficiency scale of organic compounds, Rapid Commun. Mass Sp., 22, 379–384,
660 https://doi.org/10.1002/rcm.3371, 2008.

661

662 Li, F., Zhou, S., Du, L., Zhao, J., Hang, J., and Wang, X.: Aqueous-phase chemistry of atmospheric phenolic compounds: A
663 critical review of laboratory studies, Sci. Total Environ., 856, 158895, https://doi.org/10.1016/j.scitotenv.2022.158895,
664 2022.

665

666 Li, P., Li, X., Yang, C., Wang, X., Chen, J., and Collett, J. L. Jr.: Fog water chemistry in Shanghai, Atmos. Environ., 45,
667 4034−4041, https://doi.org/10.1016/j.atmosenv.2011.04.036, 2011.

668

669 Li, X., Tao, Y., Zhu, L., Ma, S., Luo, S., Zhao, Z., Sun, N., Ge, X., and Ye, Z.: Optical and chemical properties and oxidative
670 potential of aqueous-phase products from OH and $^3C^*$-initiated photooxidation of eugenol, Atmos. Chem. Phys., 22, 7793–
671 7814, https://doi.org/10.5194/acp-22-7793-2022, 2022.

672

673 Li, Y. J., Huang, D. D., Cheung, H. Y., Lee, A. K. Y., and Chan, C. K.: Aqueous-phase photochemical oxidation and direct
674 photolysis of vanillin - a model compound of methoxy phenols from biomass burning, Atmos. Chem. Phys., 14, 2871−2885,
675 https://doi.org/10.5194/acp-14-2871-2014, 2014.

676

677 Liang, Z., Zhang, R., Gen, M., Chu, Y., and Chan, C. K.: Nitrate photolysis in mixed sucrose–nitrate–sulfate particles at
678 different relative humidities, J. Phys. Chem. A, 125, 3739–3747, https://doi.org/10.1021/acs.jpca.1c00669, 2021.

679

Lin, P., Yu, J. Z., Engling, G., and Kalberer, M.: Organosulfates in humic-like substance fraction isolated from aerosols at seven locations in East Asia: a study by ultra-high-resolution mass spectrometry, Environ. Sci. Technol., 46, 13118–13127, https://doi.org/10.1021/es303570v, 2012.

Lin, P., Fleming, L. T., Nizkorodov, S. A., Laskin, J., and Laskin, A.: Comprehensive molecular characterization of atmospheric brown carbon by high resolution mass spectrometry with electrospray and atmospheric pressure photoionization, Anal. Chem., 90, 12493–12502, https://doi.org/10.1021/acs.analchem.8b02177, 2018.

Lipari, F., Dasch, J. M., and Scruggs, W. F.: Aldehyde emissions from wood-burning fireplaces, Environ. Sci. Technol., 18, 326−330, https://doi.org/10.1021/es00123a007, 1984.

Liu, C., Chen, D., and Chen, X.: Atmospheric reactivity of methoxyphenols: a review, Environ. Sci. Technol., 56, 2897–2916, https://doi.org/10.1021/acs.est.1c06535, 2022.

Liu, Y., Lu, J., Chen, Y., Liu, Y., Ye, Z., and Ge, X.: Aqueous-phase production of secondary organic aerosols from oxidation of dibenzothiophene (DBT), Atmosphere, 11, 151, https://doi.org/10.3390/atmos11020151, 2020.

Lobodin, V. V., Marshall, A. G., and Hsu, C. S.: Compositional space boundaries for organic compounds, Anal. Chem., 84, 3410–3416, https://doi.org/10.1021/ac300244f, 2012.

Lu, J., Ge, X., Liu, Y., Chen, Y., Xie, X., Ou, Y., Ye, Z., and Chen, M.: Significant secondary organic aerosol production from aqueous-phase processing of two intermediate volatility organic compounds, Atmos. Environ., 211, 63–68, https://doi.org/10.1016/j.atmosenv.2019.05.014, 2019.

Ma, L., Guzman, C., Niedek, C., Tran, T., Zhang, Q., and Anastasio, C.: Kinetics and mass yields of aqueous secondary organic aerosol from highly substituted phenols reacting with a triplet excited state, Environ. Sci. Technol., 55, 5772–5781, https://doi.org/10.1021/acs.est.1c00575, 2021.

Mabato, B. R. G., Gen, M., Chu, Y., and Chan, C. K.: Reactive uptake of glyoxal by methylaminium-containing salts as a function of relative humidity, ACS Earth Space Chem., 3, 150–157, https://doi.org/10.1021/acsearthspacechem.8b00154, 2019.

Mabato, B. R. G., Lyu, Y., Ji, Y., Li, Y. J., Huang, D. D., Li, X., Nah, T., Lam, C. H., and Chan, C. K.: Aqueous secondary organic aerosol formation from the direct photosensitized oxidation of vanillin in the absence and presence of ammonium nitrate, Atmos. Chem. Phys., 22, 273−293, https://doi.org/10.5194/acp-22-273-2022, 2022.

Mazzoleni, L. R., Saranjampour, P., Dalbec, M. M., Samburova, V., Hallar, A. G., Zielinska, B., Lowenthal, D. H., and Kohl, S.: Identification of water-soluble organic carbon in non-urban aerosols using ultrahigh-resolution FT-ICR mass spectrometry: organic anions, Environ. Chem., 9, 285−297, https://doi.org/10.1071/EN11167, 2012.

Minero, C., Bono, F., Rubertelli, F., Pavino, D., Maurino, V., Pelizzetti, E., and Vione, D.: On the effect of pH in aromatic photonitration upon nitrate photolysis, Chemosphere, 66, 650−656, https://doi.org/10.1016/j.chemosphere.2006.07.082, 2007.

Misovich, M. V., Hettiyadura, A. P. S., Jiang, W., Zhang, Q., and Laskin, A.: Molecular-level study of the photo-oxidation of aqueous-phase guaiacyl acetone in the presence of [3]C*: formation of brown carbon products, ACS Earth Space Chem., 5, 1983−1996, https://doi.org/10.1021/acsearthspacechem.1c00103, 2021.

Munger, J. W., Jacob, D. J., Waldman, J. M., and Hoffmann, M. R.: Fogwater chemistry in an urban atmosphere, J. Geophys. Res. [Oceans], 88, 5109–5121, https://doi.org/10.1029/JC088iC09p05109, 1983.

Ning, C., Gao, Y., Zhang, H., Yu, H., Wang, L., Geng, N., Cao, R., and Chen, J.: Molecular characterization of dissolved organic matters in winter atmospheric fine particulate matters (PM2.5) from a coastal city of northeast China, Sci. Total Environ., 689, 312–321, https://doi.org/10.1016/j.scitotenv.2019.06.418, 2019.

Nolte, C. G., Schauer, J. J., Cass, G. R., and Simoneit, B. R. T.: Highly polar organic compounds present in wood smoke and in the ambient atmosphere, Environ. Sci. Technol., 35, 1912−1919, https://doi.org/10.1021/es001420r, 2001.

Nozière, B., Dziedzic, P., and Córdova, A.: Products and kinetics of the liquid-phase reaction of glyoxal catalyzed by ammonium ions (NH_4^+), J. Phys. Chem. A, 113, 231−237, https://doi.org/10.1021/jp8078293, 2009.

Nozière, B., Dziedzic, P., and Córdova, A.: Inorganic ammonium salts and carbonate salts are efficient catalysts for aldol condensation in atmospheric aerosols, Phys. Chem. Chem. Phys., 12, 3864−3872, https://doi.org/10.1039/B924443C, 2010.

Nozière, B., Fache, F., Maxut, A., Fenet, B., Baudouin, A., Fine, L., and Ferronato, C.: The hydrolysis of epoxides catalyzed by inorganic ammonium salts in water: kinetic evidence for hydrogen bond catalysis, Phys. Chem. Chem. Phys., 20, 1583−1590, https://doi.org/10.1039/C7CP06790A, 2018.

Ou, Y., Nie, D., Chen, H., Ye, Z., and Ge, X.: Characterization of products from the aqueous-phase photochemical oxidation of benzene-diols, Atmosphere, 12, 534, https://doi.org/10.3390/atmos12050534, 2021.

Pang, H., Zhang, Q., Lu, X., Li, K., Chen, H., Chen, J., Yang, X., Ma, Y., Ma, J., and Huang, C.: Nitrite-mediated photooxidation of vanillin in the atmospheric aqueous phase, Environ. Sci. Technol., 53, 14253−14263, https://doi.org/10.1021/acs.est.9b03649, 2019.

Perry, R. H., Cooks, R. G., and Noll, R. J.: Orbitrap mass spectrometry: instrumentation, ion motion and applications, Mass Spectrom. Rev., 27, 661–699, https://doi.org/10.1002/mas.20186, 2008.

Powelson, M. H., Espelien, B. M., Hawkins, L. N., Galloway, M. M., and De Haan, D. O.: Brown carbon formation by aqueous-phase carbonyl compound reactions with amines and ammonium sulfate, Environ. Sci. Technol., 48, 985−993, https://doi.org/10.1021/es4038325, 2014.

Pye, H. O. T., Nenes, A., Alexander, B., Ault, A. P., Barth, M. C., Clegg, S. L., Collett, J. L. Jr., Fahey, K. M., Hennigan, C. J., Herrmann, H., Kanakidou, M., Kelly, J. T., Ku, I., McNeill, V. F., Riemer, N., Schaefer, T., Shi, G., Tilgner, A., Walker, J. T., Wang, T., Weber, R., Xing, J., Zaveri, R. A., and Zuend, A.: The acidity of atmospheric particles and clouds, Atmos. Chem. Phys., 20, 4809–4888, https://doi.org/10.5194/acp-20-4809-2020, 2020.

Raja, S., Raghunathan, R., Yu, X., Lee, T., Chen, J., Kommalapati, R. R., Murugesan, K., Shen, X., Qingzhong, Y., Valsaraj, K. T., and Collett, J. L. Jr.: Fog chemistry in the Texas-Louisiana Gulf Coast corridor, Atmos. Environ., 42, 2048−2061, https://doi.org/10.1016/j.atmosenv.2007.12.004, 2008.

Rogge, W. F., Hildemann, L. M., Mazurek, M. A., and Cass, G. R.: Sources of fine organic aerosol. 9. Pine, oak, and synthetic log combustion in residential fireplaces, Environ. Sci. Technol., 32, 13−22, https://doi.org/10.1021/es960930b, 1998.

Romonosky, D. E., Li, Y., Shiraiwa, M., Laskin, A., Laskin, J., and Nizkorodov, S. A.: Aqueous photochemistry of secondary organic aerosol of α-Pinene and α-Humulene oxidized with ozone, hydroxyl radical, and nitrate radical, J. Phys. Chem. A, 121, 1298–1309, https://doi.org/10.1021/acs.jpca.6b10900, 2017.

778 Sagebiel, J. C., Seiber, J. N., and Woodrow, J. E.: Comparison of headspace and gas-stripping methods for determining the
779 Henry's law constant (H) for organic compounds of low to intermediate H, Chemosphere, 25, 1763–1768,
780 https://doi.org/10.1016/0045-6535(92)90017-L, 1992.

782 Schauer, J. J., Kleeman, M. J., Cass, G. R., and Simoneit, B. R. T.: Measurement of emissions from air pollution sources. 3.
783 C_1-C_{29} organic compounds from fireplace combustion of wood, Environ. Sci. Technol., 35, 1716−1728,
784 https://doi.org/10.1021/es001331e, 2001.

786 Schmidt, A-C., Herzschuh, R., Matysik, F-M., and Engewald, W.: Investigation of the ionisation and fragmentation
787 behaviour of different nitroaromatic compounds occurring as polar metabolites of explosives using electrospray ionisation
788 tandem mass spectrometry, Rapid Commun. Mass Sp., 20, 2293–2302, https://doi.org/10.1002/rcm.2591, 2006.

790 Shapiro, E. L., Szprengiel, J., Sareen, N., Jen, C. N., Giordano, M. R., and McNeill, V. F.: Light-absorbing secondary
791 organic material formed by glyoxal in aqueous aerosol mimics, Atmos. Chem. Phys., 9, 2289−2300,
792 https://doi.org/10.5194/acp-9-2289-2009, 2009.

794 Siegmann, K. and Sattler, K.: Formation mechanism for polycyclic aromatic hydrocarbons in methane flames, J. Chem.
795 Phys., 112, 698–709, https://doi.org/10.1063/1.480648, 2000.

797 Simoneit, B. R. T.: Biomass burning — a review of organic tracers for smoke from incomplete combustion, Appl.
798 Geochem., 17, 129–162, https://doi.org/10.1016/S0883-2927(01)00061-0, 2002.

800 Simoneit, B. R. T., Rogge, W. F., Mazurek, M. A., Standley, L. J., Hildemann, L. M., and Cass, G. R.: Lignin pyrolysis
801 products, lignans, and resin acids as specific tracers of plant classes in emissions from biomass combustion, Environ. Sci.
802 Technol., 27, 2533−2541, https://doi.org/10.1021/es00048a034, 1993.

804 Simoneit, B. R. T., Schauer, J. J., Nolte, C. G., Oros, D. R., Elias, V. O., Fraser, M. P., Rogge, W. F., and Cass, G. R.:
805 Levoglucosan, a tracer for cellulose in biomass burning and atmospheric particles, Atmos. Environ., 33, 173−182,
806 https://doi.org/10.1016/S1352-2310(98)00145-9, 1999.

808 Simpson, C. D., Paulsen, M., Dills, R. L., Liu, L.-J. S., and Kalman, D. A.: Determination of methoxyphenols in ambient
809 atmospheric particulate matter: tracers for wood combustion, Environ. Sci. Technol., 39, 631−637,
810 https://doi.org/10.1021/es0486871, 2005.

812 Slikboer, S., Grandy, L., Blair, S. L., Nizkorodov, S. A., Smith, R. W., and Al-Abadleh, H. A.: Formation of light absorbing
813 soluble secondary organics and insoluble polymeric particles from the dark reaction of catechol and guaiacol with Fe(III),
814 Environ. Sci. Technol., 49, 7793–7801, https://doi.org/10.1021/acs.est.5b01032, 2015.

816 Smith, D. F., Kleindienst, T. E., and McIver, C. D.: Primary product distributions from the reaction of OH with m-, p-xylene,
817 1,2,4-and 1,3,5-trimethylbenzene, J. Atmos. Chem., 34, 339–364, https://doi.org/10.1023/A:1006277328628, 1999.

819 Smith, J. D., Sio, V., Yu, L., Zhang, Q., and Anastasio, C.: Secondary organic aerosol production from aqueous reactions of
820 atmospheric phenols with an organic triplet excited state, Environ. Sci. Technol., 48, 1049–1057,
821 https://doi.org/10.1021/es4045715, 2014.

823 Smith, J. D., Kinney, H., and Anastasio, C.: Aqueous benzene-diols react with an organic triplet excited state and hydroxyl
824 radical to form secondary organic aerosol, Phys. Chem. Chem. Phys., 17, 10227−10237,
825 https://doi.org/10.1039/C4CP06095D, 2015.

827 Smith, J. D., Kinney, H., and Anastasio, C.: Phenolic carbonyls undergo rapid aqueous photodegradation to form low-
828 volatility, light-absorbing products, Atmos. Environ., 126, 36−44, https://doi.org/10.1016/j.atmosenv.2015.11.035, 2016.
829
830 Song, J., Li, M., Jiang, B., Wei, S., Fan, X., and Peng, P.: Molecular characterization of water-soluble humic like substances
831 in smoke particles emitted from combustion of biomass materials and coal using ultrahigh-resolution electrospray ionization
832 Fourier transform ion cyclotron resonance mass spectrometry, Environ. Sci. Technol., 52, 2575–2585,
833 https://doi.org/10.1021/acs.est.7b06126, 2018.
834
835 Sun, Y. L., Zhang, Q., Anastasio, C., and Sun, J.: Insights into secondary organic aerosol formed via aqueous-phase
836 reactions of phenolic compounds based on high resolution mass spectrometry, Atmos. Chem. Phys., 10, 4809−4822,
837 https://doi.org/10.5194/acp-10-4809-2010, 2010.
838
839 US EPA: Estimation Programs Interface Suite™ for Microsoft® Windows, v 4.1, United States Environmental Protection
840 Agency, Washington, DC, USA, 2012.
841
842 Wang, K., Huang, R-J., Brüggemann, M., Zhang, Y., Yang, L., Ni, H., Guo, J., Wang, M., Han, J., Bilde, M., Glasius, M.,
843 and Hoffmann, T.: Urban organic aerosol composition in eastern China differs from north to south: molecular insight from a
844 liquid chromatography–mass spectrometry (Orbitrap) study, Atmos. Chem. Phys., 21, 9089–9104,
845 https://doi.org/10.5194/acp-21-9089-2021, 2021.
846
847 Wang, X., Hayeck, N., Brüggemann, M., Yao, L., Chen, H., Zhang, C., Emmelin, C., Chen, J., George, C., and Wang, L.:
848 Chemical characterization of organic aerosols in Shanghai: A study by ultrahigh-performance liquid chromatography
849 coupled with orbitrap mass spectrometry, J. Geophys. Res. Atmos., 122, 11703–11722,
850 https://doi.org/10.1002/2017JD026930, 2017.
851
852 Wang, Y., Huang, D. D., Huang, W., Liu, B., Chen, Q., Huang, R., Gen, M., Mabato, B. R. G., Chan, C. K., Li, X., Hao, T.,
853 Tan, Y., Hoi, K. I., Mok, K. M., and Li, Y. J.: Enhanced nitrite production from the aqueous photolysis of nitrate in the
854 presence of vanillic acid and implications for the roles of light-absorbing organics, Environ. Sci. Technol., 55, 15694−15704,
855 https://doi.org/10.1021/acs.est.1c04642, 2021.
856
857 Wang, Y., Huang, W., Tian, L., Wang, Y., Li, F., Huang, D. D., Zhang, R., Mabato, B. R. G., Huang, R., Chen, Q., Ge, X.,
858 Du, L., Ma, Y. G., Gen, M., Hoi, K. I., Mok, K. M., Yu, J. Z., Chan, C. K., Li, X., and Li, Y. J.: Decay kinetics and
859 absorption changes of methoxyphenols and nitrophenols during nitrate-mediated aqueous photochemical oxidation at 254
860 and 313 nm, ACS Earth Space Chem., 6, 1115−1125, https://doi.org/10.1021/acsearthspacechem.2c00021, 2022.
861
862 Yang, J., Au, W. C., Law, H., Leung, C. H., Lam, C. H, and Nah, T.: pH affects the aqueous-phase nitrate-mediated
863 photooxidation of phenolic compounds: implications for brown carbon formation and evolution, Environ. Sci.: Processes
864 Impacts, https://doi.org/10.1039/D2EM00004K, 2022.
865
866 Yasmeen, F., Vermeylen, R., Szmigielski, R., Iinuma, Y., Böge, O., Herrmann, H., Maenhaut, W., and Claeys, M.:
867 Terpenylic acid and related compounds: precursors for dimers in secondary organic aerosol from the ozonolysis of α and β-
868 pinene, Atmos. Chem. Phys., 10, 9383–9392, https://doi.org/10.5194/acp-10-9383-2010, 2010.
869
870 Yaws, C. L.: Handbook of vapor pressure, volume 3: Organic compounds C8 to C28, Gulf Professional Publishing, 1994.
871
872 Ye, Z., Qu, Z., Ma, S., Luo, S., Chen, Y., Chen, H., Chen, Y., Zhao, Z., Chen, M., and Ge, X.: A comprehensive
873 investigation of aqueous-phase photochemical oxidation of 4-ethylphenol, Sci. Total Environ., 685, 976–985,
874 https://doi.org/10.1016/j.scitotenv.2019.06.276, 2019.
875

876 Yu, G., Bayer, A. R., Galloway, M. M., Korshavn, K. J., Fry, C. G., and Keutsch, F. N.: Glyoxal in aqueous ammonium
877 sulfate solutions: products, kinetics and hydration effects, Environ. Sci. Technol., 45, 6336−6342,
878 https://doi.org/10.1021/es200989n, 2011.

880 Yu, L., Smith, J., Laskin, A., Anastasio, C., Laskin, J., and Zhang, Q.: Chemical characterization of SOA formed from
881 aqueous-phase reactions of phenols with the triplet excited state of carbonyl and hydroxyl radical, Atmos. Chem. Phys., 14,
882 13801−13816, https://doi.org/10.5194/acp-14-13801-2014, 2014.

884 Yu, L., Smith, J., Laskin, A., George, K. M., Anastasio, C., Laskin, J., Dillner, A. M., and Zhang, Q.: Molecular
885 transformations of phenolic SOA during photochemical aging in the aqueous phase: competition among oligomerization,
886 functionalization, and fragmentation, Atmos. Chem. Phys., 16, 4511−4527, https://doi.org/10.5194/acp-16-4511-2016.

888 Zhang, Q. and Anastasio, C.: Conversion of fogwater and aerosol organic nitrogen to ammonium, nitrate, and NO_x during
889 exposure to simulated sunlight and ozone, Environ. Sci. Technol., 37, 3522–3530, https://doi.org/10.1021/es034114x, 2003.

891 Zhang, R., Gen, M., Huang, D. D., Li, Y. J., and Chan, C. K.: Enhanced sulfate production by nitrate photolysis in the
892 presence of halide ions in atmospheric particles, Environ. Sci. Technol., 54, 3831–3839,
893 https://doi.org/10.1021/acs.est.9b06445, 2020.

895 Zhang, R., Gen, M., Fu, T-M., and Chan, C. K.: Production of formate via oxidation of glyoxal promoted by particulate
896 nitrate photolysis, Environ. Sci. Technol., 55, 5711–5720, https://doi.org/10.1021/acs.est.0c0819, 2021.

898 Zhang, R., Gen, M., Liang, Z., Li, Y. J., and Chan, C. K.: Photochemical reactions of glyoxal during particulate ammonium
899 nitrate photolysis: Brown carbon formation, enhanced glyoxal decay, and organic phase formation, Environ. Sci. Technol.,
900 56, 1605–1614, https://doi.org/10.1021/acs.est.1c07211, 2022.

902 Zielinski, T., Bolzacchini, E., Cataldi, M., Ferrero, L., Graßl, S., Hansen, G., Mateos, D., Mazzola, M., Neuber, R., Pakszys,
903 P., Posyniak, M., Ritter, C., Severi, M., Sobolewski, P., Traversi, R., and Velasco-Merino, C.: Study of chemical and optical
904 properties of biomass burning aerosols during long-range transport events toward the Arctic in summer 2017, Atmosphere,
905 11, 84, https://doi.org/10.3390/atmos11010084, 2020.

906
907
908
909
910

911

912

913

914

915

916

917

918

919

920

921

922

Table 1. Reaction conditions, initial GUA (and DMB or VL) decay rate constants, normalized abundance of products, average elemental ratios, and average carbon oxidation state ($\langle OS_C \rangle$) in each experiment. The reaction systems consisted of GUA (0.1 mM), DMB (0.01 mM), VL (0.01 mM), and AN (1 mM) under air-saturated conditions after 180 min of simulated sunlight irradiation. The UHPLC-HESI-Orbitrap-MS data were obtained in both positive (POS) and negative (NEG) ion modes.

Exp no.	Reaction conditions	Initial GUA (and DMB or VL) decay rate constants (min^{-1}/s^{-1})[a]	Normalized abundance of products[b]	Normalized abundance of N-containing compounds[b]	$\langle O:C \rangle$[c]	$\langle H:C \rangle$[c]	$\langle N:C \rangle$[c]	$\langle OS_C \rangle$[c]
1	GUA+DMB	GUA: 6.3 ± 0.25 DMB: 0.78 ± 0.10	376 ± 22	NA	POS: 0.34	0.91	NA	-0.22
					NEG: 0.40	0.94	NA	-0.15
2	GUA+ DMB+AN	GUA: 5.3 ± 0.50 DMB: 0.69 ± 0.052	310 ± 4	114	POS: 0.28	0.94	0.12	-0.03
					NEG: 0.37	0.91	0.04	-0.05
3	GUA+VL	GUA: 1.5 ± 0.14 VL: 3.6 ± 0.55	94 ± 5	NA	POS: 0.41	0.91	NA	-0.10
					NEG: 0.40	0.94	NA	-0.14
4	GUA+ VL+AN	GUA: 1.6 ± 0.12 VL: 2.9 ± 0.032	100 ± 2	8	POS: 0.31	1.02	0.02	-0.34
					NEG: 0.39	0.91	0.03	-0.02
5	GUA+AN	0.57 ± 0.036	23 ± 1	9	POS: 0.35	0.99	0.16	0.19
					NEG: 0.38	1.01	0.05	-0.08

929

[a]The data fitting was performed in the initial linear region. Each value is the average of results from triplicate experiments, corrected for internal light screening due to DMB, VL, and AN, and normalized to the experimental photon flux. Errors represent one standard deviation. [b]The normalized product abundance was calculated using the data from UHPLC-HESI-Orbitrap-MS in the positive (POS) ion mode as the GUA signal from the negative (NEG) ion mode was weak, which may introduce significant uncertainties during normalization. The uncertainties were propagated from the changes in [GUA] measured using UHPLC-PDA and the MS signal intensities. The samples for experiments without AN (marked with NA) were not analyzed for N-containing compounds. [c]The average elemental ratios ($\langle O:C \rangle$, $\langle H:C \rangle$, and $\langle N:C \rangle$) and $\langle OS_C \rangle$ were based on the UHPLC-HESI-Orbitrap-MS results and estimated using the signal-weighted method (Bateman et al., 2012). The OS_C of GUA, DMB, and VL are -0.57, -0.44, and -0.25, respectively.

939

940

941

942

943

944
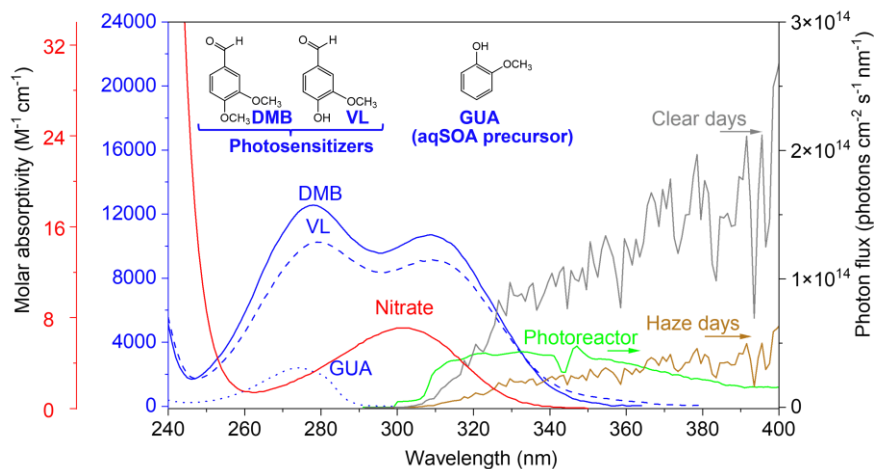
Figure 1. The base-10 molar absorptivities (M^{-1} cm^{-1}) of 3,4-dimethoxybenzaldehyde (DMB, blue solid line), vanillin (VL, blue dashed line), guaiacol (GUA, blue dotted line), and nitrate (red solid line). The green line is the photon flux in the aqueous photoreactor. The gray and brown lines are the photon fluxes on typical clear and haze days, respectively, in Beijing, China (Mabato et al., 2022). The top of the figure also shows the structures of DMB, VL, and GUA.
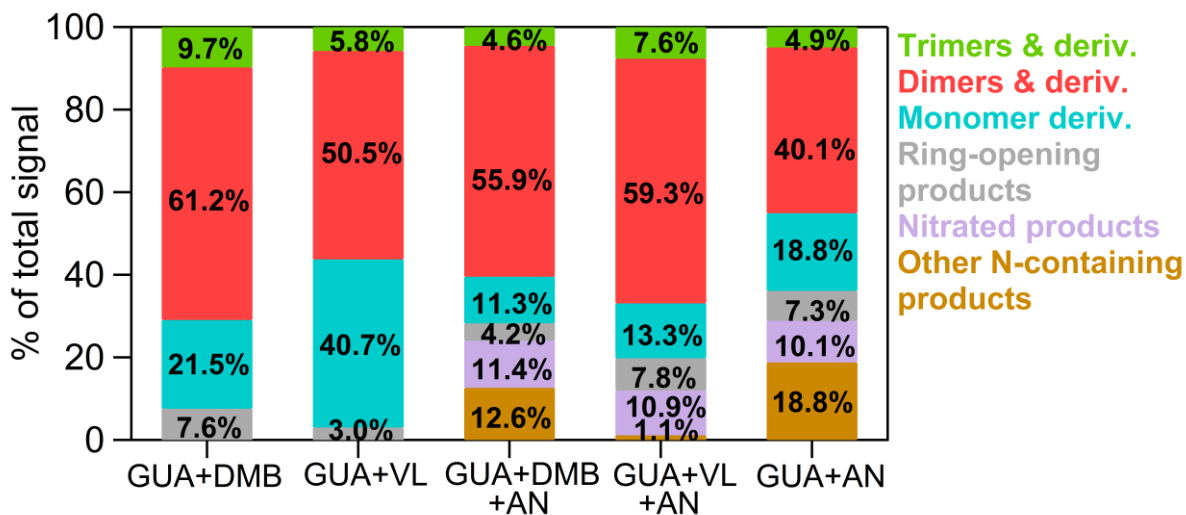
Figure 2. Signal-weighted distributions of aqSOA from GUA+DMB, GUA+VL, GUA+DMB+AN, GUA+VL+AN, and GUA+AN. These product distributions were calculated from combined UHPLC-HESI-Orbitrap-MS data obtained in positive (POS) and negative (NEG) ion modes. The values indicate the contribution of different product classifications to the total signals for each reaction condition.
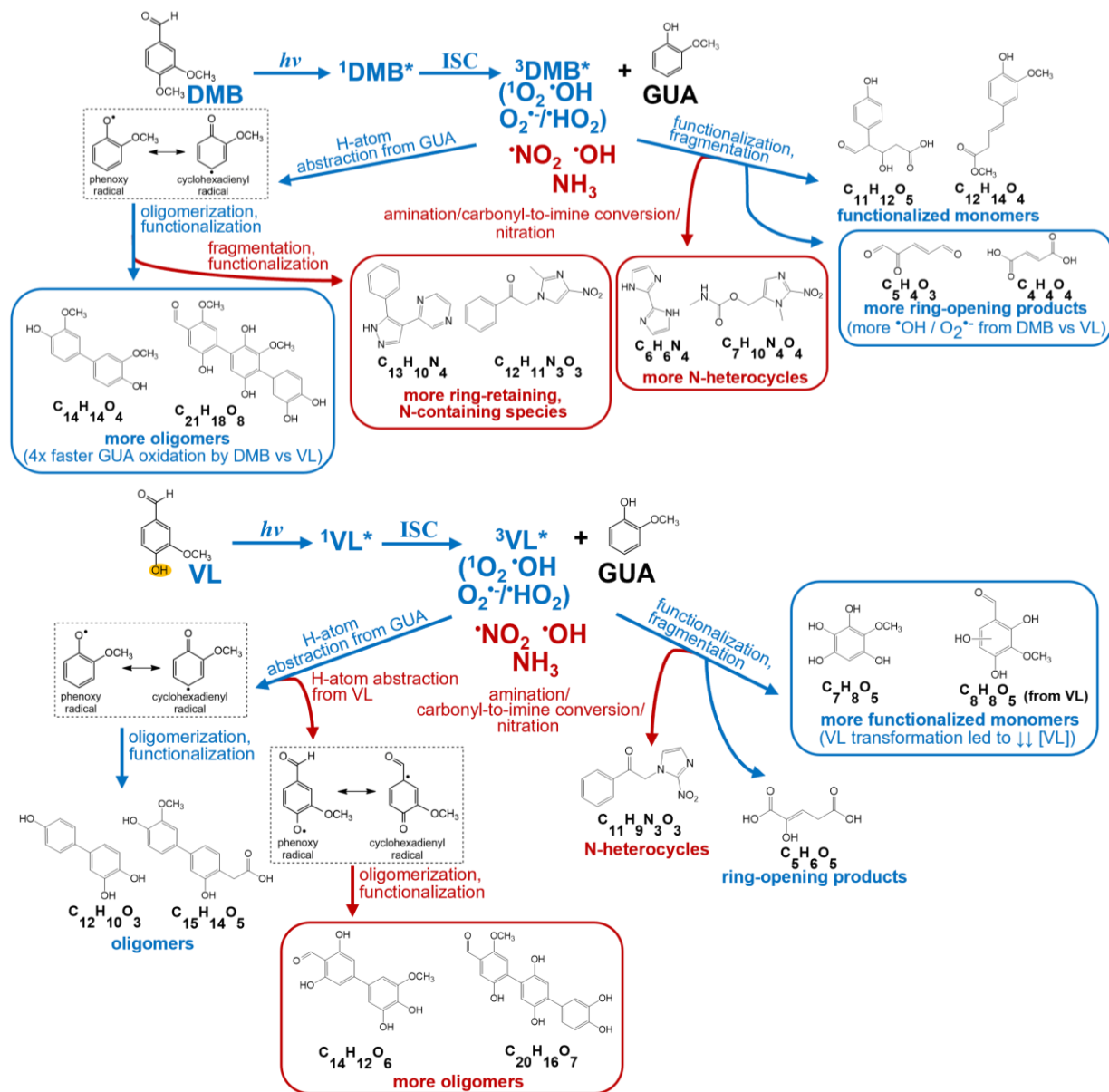
Figure 3. Summary of the main differences between photosensitized GUA oxidation by ^{3}DMB* (top) and ^{3}VL* (bottom) in the absence (blue labels and boxes) and presence (red labels and boxes) of ammonium nitrate at pH 4 under air-saturated conditions. Boxed structures indicate product classifications with notable differences. DMB and VL absorb light and are promoted to their singlet excited states (^{1}DMB* and ^{1}VL*), which then undergo intersystem crossing (ISC) to form ^{3}DMB* and ^{3}VL*. Secondary oxidants (^{1}O$_2$, O$_2$$^{•-}$/$^•HO_2$, $^•$OH) can be formed from ^{3}DMB* and ^{3}VL* upon reactions with O$_2$ and GUA (George et al., 2018; Chen et al., 2020; Misovich et al., 2021; Mabato et al., 2022). The structures shown are examples of the major products (Tables S1 to S4) for different product classifications.

Figure 4. (a) Increase in light absorption throughout 180 min of irradiation for all reaction systems studied and (b) Change in the rate of sunlight absorption (ΔR_{abs}) from 350-550 nm at 180 min during typical clear and haze days in Beijing, China for aqSOA from GUA+DMB+AN, GUA+DMB, GUA+VL+AN, GUA+VL, and GUA+AN. Error bars represent one standard deviation of triplicate experiments.

1 **Supplementary material**

3 **Comparison of aqueous SOA product distributions from**
4 **guaiacol oxidation by non-phenolic and phenolic**
5 **methoxybenzaldehydes as photosensitizers in the absence and**
6 **presence of ammonium nitrate**

8 Beatrix Rosette Go Mabato[1,2], Yong Jie Li[3], Dan Dan Huang[4], Yalin Wang[3], and Chak K.
9 Chan[1,2]*

11 [1]School of Energy and Environment, City University of Hong Kong, Hong Kong, China

12 [2]City University of Hong Kong Shenzhen Research Institute, Shenzhen, China

13 [3]Department of Civil and Environmental Engineering, and Centre for Regional Ocean,

14 Faculty of Science and Technology, University of Macau, Macau, China

15 [4]Shanghai Academy of Environmental Sciences, Shanghai 200233, China

18

20 *Correspondence to*: Chak K. Chan (Chak.K.Chan@cityu.edu.hk)

22
23
24
25
26
27
28
29
30

Section S1. UHPLC-PDA analyses

An ultra-high performance liquid chromatography system (UHPLC, Waters Acquity H-Class, Waters, Milford, USA) coupled to a photodiode array (PDA) detector (Waters, Milford, USA) was used for the quantification of GUA, DMB, and VL concentrations. The samples were first filtered through a 0.2 μm Chromafil® Xtra PTFE filter (Macherey-Nagel GmbH & Co. KG, Germany). The separation of products was conducted using an Acquity HSS T3 column (1.8 μm, 2.1 mm × 100 mm; Waters Corp.). The column oven was held at 30 °C, and the autosampler was cooled at 4 °C. The injection volume was set to 5 μL. The binary mobile phase was composed of water (A) and acetonitrile (B). The gradient elution was performed at a flow rate of 0.2 mL/min: 0–1 min, 10% eluent B; 1–25 min, linear increase to 90% eluent B; 25–29.9 min, hold 90% eluent B; 29.9–30 min, decrease to 10% eluent B; 30–35 min, re-equilibrate at 10% eluent B for 5 min. GUA, DMB, and VL were analyzed using the channels with UV absorption at 274, 274, and 300 nm, respectively.

Section S2. UHPLC-HESI-Orbitrap-MS analyses

A Thermo Orbitrap Fusion Lumos Mass Spectrometry (Thermo Fisher Scientific, Waltham, MA, USA) connected to a Thermo Scientific UltiMate 3000 UHPLC system (Thermo Fisher Scientific, Waltham, MA, USA) via heated electrospray ionization (HESI) as the interface (UHPLC-HESI-Orbitrap-MS) was used to characterize the reaction products. The mobile phases used were 0.1% (v/v) formic acid (in milli-Q water) (A) and acetonitrile (B). The same settings (e.g., column, gradient, oven temperature) used in the UHPLC-PDA (Sect. S1) were applied in the UHPLC-HESI-Orbitrap-MS system. The HESI-MS spectra were acquired in both positive and negative ion modes. The HESI parameters were as follows: Spray voltage, 2500 V for both positive and negative HESI; sheath gas, 35 arbitrary units; nebulizer auxiliary gas, 10 arbitrary units; sweep gas, 3 arbitrary units. General instrumental parameters were set as follows: ion transfer tube temperature, 320 °C; vaporizer temperature, 350 °C. The mass

range for full scan MS was set at 50-1000 m/z with a mass resolution of 60,000 at 200 m/z. The automatic gain control (AGC) target was 4.0×10^5 with a maximum injection time of 50 ms. The UHPLC-HESI-Orbitrap-MS data obtained in positive and negative ion modes were pretreated using Progenesis QI (version 2.4; Nonlinear Dynamics) for peak picking and alignment. Most peaks detected in the blank (~99% for all experiments) were excluded from the samples except for peaks with a minimum of 2.5 times greater intensity in the sample spectrum than in the blank (Laskin et al., 2014). In addition, a peak was considered a product if the difference in the peak area between the samples before and after irradiation is ≥10 times. In this work, two independently prepared samples for each reaction condition were analyzed using the UHPLC-HESI-Orbitrap-MS. Only peaks that were reproducibly detected in both sets of samples were retained. The formula assignments were carried out using the MIDAS molecular formula calculator (http://magnet.fsu.edu/~midas/) with the following constraints: C ≤100, H ≤150, O ≤30, and N ≤10, and mass error of 10 ppm. The nitrogen atom was excluded in the constraints for experiments without AN. The ChemSpider database (Royal Society of Chemistry) was also queried to return valid molecules that may be useful for proposing product structures. Overall, the proposed structures in this work are based on the molecular formulas, DBE values, and structural and mechanistic information provided in earlier similar works on methoxyphenols (Yee et al., 2013; Li et al., 2014; Yu et al., 2014, 2016; He et al., 2019; Chen et al., 2020; Jiang et al., 2021; Misovich et al., 2021; Mabato et al., 2022). For clarity, the formulas discussed in this work correspond to neutral analytes (e.g., with H^+ or NH_4^+ removed from the ion formula).

The double bond equivalent (DBE) values (Koch and Dittmar, 2006) and carbon oxidation state (OS_C; Kroll et al., 2011, 2015; Lv et al., 2016) of the neutral formulas were calculated using the following equations:

82    $DBE = C - H/2 + N/2 + 1$ (Eq. S1)

83    $OS_C = 2 \times O/C + 3 \times N/C - H/C$ (Eq. S2)

84   where C, H, O, and N correspond to the number of carbon, hydrogen, oxygen, and nitrogen

85   atoms in the neutral formula. Moreover, the average oxygen to carbon (O:C) ratios, $\langle O:C \rangle$:

86   ($\langle O:C \rangle = \sum_i(abundance_i)O_i / \sum_i(abundance_i)C_i$), average nitrogen to carbon (N:C) ratios,

87    $\langle N:C \rangle$: ($\langle N:C \rangle = \sum_i(abundance_i)N_i / \sum_i(abundance_i)C_i$), and average hydrogen to carbon

88   (H:C) ratios, $\langle H:C \rangle$: ($\langle H:C \rangle = \sum_i(abundance_i)H_i / \sum_i(abundance_i)C_i$) after the reactions

89   were further estimated using the signal-weighted method (Bateman et al., 2012). The average

90   OS_C, $\langle OS_C \rangle$ was also calculated as follows:

91    $\langle OS_C \rangle = 2 \times \langle O:C \rangle + 3 \times \langle N:C \rangle - \langle H:C \rangle$ (Eq. S3)

92   **Section S3. IC analyses of small organic acids**

93   An ion chromatography system (IC, Dionex ICS-1100, Sunnyvale, CA) equipped with a

94   Dionex AS-DV autosampler (Sunnyvale, CA) enabled the analyses of small organic acids. The

95   separation was achieved using an IonPac™ AS11 column (4 × 250 mm) with an IonPac™

96   AG11 guard column (4 × 50 mm). The isocratic elution was applied at a 1.0 mL/min flow rate

97   with 12 mM sodium hydroxide (NaOH) as the eluent. The total run time was set at 10 min. The

98   standard solutions (1–50 μM) of formic, succinic, and oxalic acid were analyzed three times

99   along with the samples and water blank. Formic, succinic, and oxalic acid had retention times

100   of 1.9 min, 3.7 min, and 5.9 min, respectively.

101   **Section S4. UV-Vis spectrophotometric analyses**

102   A UV-Vis spectrophotometer (UV-3600, Shimadzu Corp., Japan) was used to measure the

103   absorbance changes for the samples. The absorbance values from 200 to 700 nm were measured

104   instantly after sample collection, and measurements were done in triplicate. The change in the

105   integrated area of absorbance from 350 to 550 nm was used to represent the absorbance

106   enhancements. The increase of light absorption at this wavelength range, where GUA, DMB,

107 ~~and VL~~ did not initially absorb light and where DMB and VL have little absorption, suggests

108 the formation of light-absorbing products (Smith et al., 2016).

Section S5. Further discussions on van Krevelen diagrams and OS_C vs. n_C plots for

GUA+DMB and GUA+VL aqSOA

111 Consistent with the higher contribution of ring-opening species, GUA+DMB had more

112 products with H:C ≥1.5 and O:C ≤0.5 (Fig. S5a–b), possibly due to more oxygenated aliphatic

113 species. GUA+VL (Fig. S5c–d) also had high-relative-abundance products with H:C of ~1 and

114 O:C ≥0.5. Similar to our previous work (0.1 mM GUA + 0.1 mM VL; Mabato et al., 2022), the

115 two high-relative-abundance species with O:C ≥0.5 were associated with hydroxylated

116 products ($C_7H_8O_4$ and $C_8H_8O_5$, #28 and 35; Table S2) that were also observed in earlier works

117 on $^3DMB^*$ and $^{\bullet}OH$-mediated oxidation (Yu et al., 2014, 2016). These hydroxylated products

118 were also present in GUA+DMB but with lower relative abundance. Triplet-mediated phenol

119 oxidation can generate H_2O_2 (Anastasio et al., 1997), a photolytic source of $^{\bullet}OH$. Indeed,

120 hydroxylation is significant in aqueous-phase phenol oxidation (Li et al., 2014; Yu et al., 2014,

121 2016; Chen et al., 2020; Jiang et al., 2021; Misovich et al., 2021; Mabato et al., 2022).

122 The OS_C vs. n_C plots for both GUA+DMB and GUA+VL display high-relative-

123 abundance species clustered at n_C of 12 to 15 and OS_C >-1, which can be ascribed to dimers

124 and derivatives (Fig. S6a–d). The species with n_C >15 had the highest DBE values and can be

125 attributed to trimers. These compounds were more abundant in GUA+DMB, likely due to the

126 greater extent of photosensitized reactions by $^3DMB^*$ compared to $^3VL^*$. Indeed,

127 oligomerization is an important process in aqSOA formation via triplet-mediated oxidation (Yu

128 et al., 2014, 2016; Chen et al., 2020; Jiang et al., 2021; Misovich et al., 2021; Mabato et al.,

129 2022). As indicated by the higher quantity of low DBE species, ring-opening and fragmentation

130 pathways were more extensive in GUA+DMB. In GUA+VL, there were also high-relative-

131 abundance products with n_C <10, OS_C ≥0, and DBE <5, corresponding to the hydroxylated

132 products mentioned earlier.

Section S6. Estimation of the apparent quantum efficiency of guaiacol photodegradation

134 The apparent quantum efficiency of GUA photodegradation (φ_{GUA}) in the presence of DMB,

135 VL, or nitrate during simulated sunlight illumination can be defined as (Anastasio et al., 1997;

136 Smith et al., 2014, 2016):

137 $$\Phi_{GUA} = \frac{\text{mol GUA destroyed}}{\text{mol photons absorbed}} \qquad \text{(Eq. S4)}$$

138 Φ_{GUA} was calculated using the measured rate of GUA decay and rate of light absorption by

139 DMB, VL, or nitrate through the following equation:

140 $$\Phi_{GUA} = \frac{\text{rate of GUA decay}}{\text{rate of light absorption by DMB or VL or nitrate}} = \frac{k'_{GUA} \times [GUA]}{\sum[(1-10^{-\varepsilon_\lambda[C]l}) \times I'_\lambda]} \qquad \text{(Eq. S5)}$$

141 where k'_{GUA} is the pseudo-first-order rate constant for GUA decay, [GUA] is the concentration

142 of GUA (M), ε_λ is the base-10 molar absorptivity (M^{-1} cm^{-1}) of DMB, VL, or nitrate at

143 wavelength λ, [C] is the concentration of DMB, VL, or nitrate (M), l is the pathlength of the

144 illumination cell (cm), and I'_λ is the volume-averaged photon flux (mol-photons L^{-1} s^{-1} nm^{-1})

145 determined from 2NB actinometry:

146 $$j(2NB) = 2.303 \times \Phi_{2NB} \times l \times \Sigma_{300\,nm}^{350\,nm}(\varepsilon_{2NB,\lambda} \times I'_\lambda \times \Delta\lambda) \qquad \text{(Eq. S6)}$$

147 where j(2NB) is the decay rate constant of 2-nitrobenzaldehyde (2NB), the chemical

148 actinometer used to determine the photon flux in the aqueous photoreactor, $\Phi_{2NB,\lambda}$ and $\varepsilon_{2NB,\lambda}$

149 are the quantum yield (molecule $photon^{-1}$) and base-10 molar absorptivity (M^{-1} cm^{-1}) for 2NB,

150 respectively, and $\Delta\lambda$ is the wavelength interval between actinic flux data points (nm).

Section S7. Further discussions on van Krevelen diagrams and OS_c vs. n_C plots for

152 **GUA+DMB+AN, GUA+VL+AN, and GUA+AN aqSOA**

153 The position of the CHO, CHON, and CHN species in the van Krevelen diagrams for

154 GUA+DMB+AN and GUA+VL+AN broadly resembled those of CHO species in the absence

155 of AN (Fig. S5). The CHON species for GUA+DMB+AN and GUA+VL+AN mostly had O:C

156 ratios <0.7, consistent with previous studies on BBOA e.g., wheat straw burning in K-Puszta

157 in the Great Hungarian Plain of Hungary, biomass burning at Canadian rural sites such as Saint

158 Anicet, and BBOA from Amazonia (Schmitt-Kopplin et al., 2010; Claeys et al., 2012;

159 Kourtchev et al., 2017).

160 The CHN species in GUA+DMB+AN and GUA+VL+AN appeared to have analogous

161 H:C ratios. GUA+DMB+AN had ~2 times more CHON and CHN species than GUA+VL+AN,

162 and there were more of these species with higher abundance in the former, indicating a greater

163 extent of reactions with AN. The high-relative-abundance products for GUA+DMB+AN and

164 GUA+VL+AN were similar to those in the absence of AN, except the hydroxylated products

165 (e.g., $C_7H_8O_4$; #28; Table S2) previously mentioned for GUA+VL. Among the high-relative-

166 abundance products for GUA+DMB+AN was a CHN species with H:C of ~0.8. For

167 GUA+VL+AN, the high-relative-abundance products include two CHON species with O:C

168 and H:C ratios of 0.3-0.6 and 0.6-0.8. The major difference between GUA+AN and

169 GUA+DMB+AN/GUA+VL+AN was the presence of more high-relative-abundance CHON

170 and CHN species (Fig. S9) in GUA+AN which can be expected given that AN was the only

171 source of oxidants in this case. Compared to GUA+AN, more species (CHO, CHON, and

172 CHN) were observed for GUA+DMB+AN and GUA+VL+AN, attributable to contributions

173 from both photosensitization and (ammonium) nitrate photolysis.

174 Moreover, GUA+DMB+AN and GUA+VL+AN aqSOA had mainly similar features in

175 the OS_C vs. n_C plots as those observed in the absence of AN (Fig. S6). GUA+DMB+AN and

176 GUA+VL+AN aqSOA also had more CHON and CHN species with higher OS_C, n_C, and DBE

177 (Fig. S6e–h) relative to GUA+AN (Fig. S10), indicating more conjugated N-containing

178 compounds. For GUA+DMB+AN and GUA+VL+AN, the CHON and CHN species had a

179 wider range of OS_C compared to CHO species (Fig. S6e–h). The high-relative-abundance

180   species (n_C of 12 to 15 and OS_C >-1) corresponded to dimers and trimers similar to those noted

181   in the absence of AN, along with some N-containing species. These include a CHN species

182   with n_C of 13, OS_C ~0, and 11 DBE for GUA+DMB+AN, and 2 CHON species with n_C of 5

183   and 11, OS_C of 2.5 and 1, and 6 and 9 DBE for GUA+VL+AN.

184

185

186
187
188
189
190
191
192
193
194
195
196
197
198
199
200
201
202
203
204
205
206
207
208
209
210
211
212
213
214
215
216
217
218
219
220
221
222
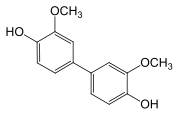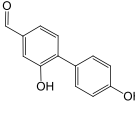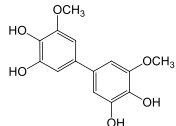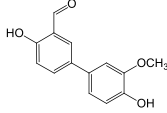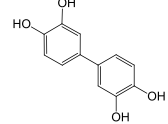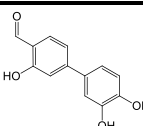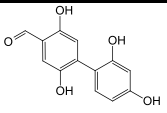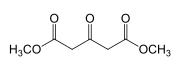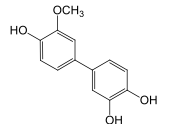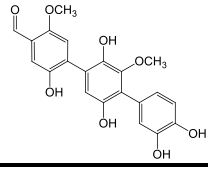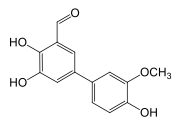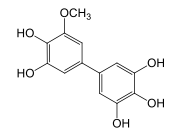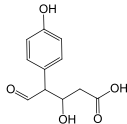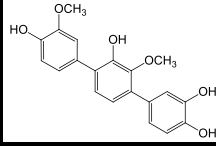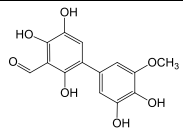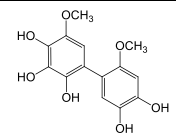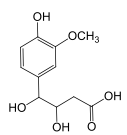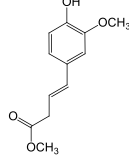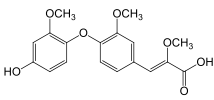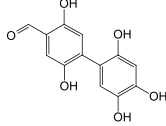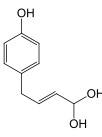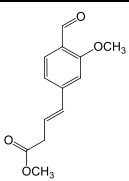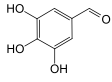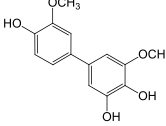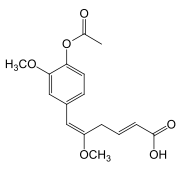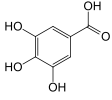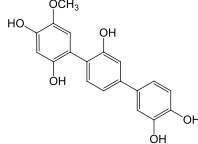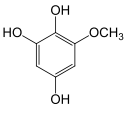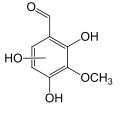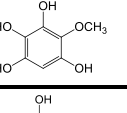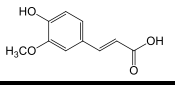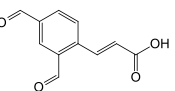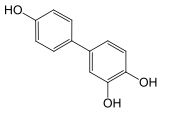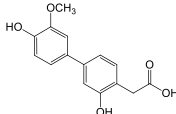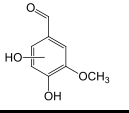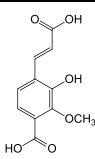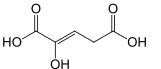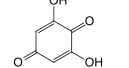
223 **Table S1**. Possible structures of the major products detected from GUA+DMB using UHPLC-
224 HESI-Orbitrap-MS operated in positive (POS) and negative (NEG) ion modes.
225

No.	GUA+DMB POS Molecular formula and exact mass	DBE	Possible structure	No.	GUA+DMB NEG Molecular formula and exact mass	DBE	Possible structure
1	$C_{14}H_{14}O_4$ (246.0892)	8	*(structure)*		$C_{14}H_{14}O_4$ (246.0892) (No. 1; GUA+DMB POS)		
2	$C_{13}H_{10}O_3$ (214.0630)	9	*(structure)*	16	$C_{14}H_{14}O_6$ (278.0790)	8	*(structure)*
3	$C_{14}H_{12}O_4$ (244.0736)	9	*(structure)*	17	$C_{12}H_{10}O_4$ (218.0579)	8	*(structure)*
4	$C_{13}H_{10}O_4$ (230.0579)	9	*(structure)*		$C_{13}H_{12}O_4$ (232.0736) (No. 6; GUA+DMB POS)		
5	$C_{13}H_{10}O_5$ (246.0528)	9	*(structure)*	18	$C_7H_{10}O_5$ (174.0528)	3	*(structure)*
6	$C_{13}H_{12}O_4$ (232.0736)	8	*(structure)*	19	$C_{21}H_{18}O_8$ (398.1002)	13	*(structure)*
7	$C_{14}H_{12}O_5$ (260.0685)	9	*(structure)*	20	$C_{13}H_{12}O_6$ (264.0634)	8	*(structure)*
8	$C_{11}H_{12}O_5$ (224.0685)	6	*(structure)*	21	$C_{20}H_{18}O_6$ (354.1103)	12	*(structure)*
9	$C_{14}H_{12}O_7$ (292.0583)	9	*(structure)*	22	$C_{14}H_{14}O_7$ (294.0740)	8	*(structure)*
10	$C_{11}H_{14}O_6$ (242.0790)	5	*(structure)*	23	$C_{12}H_{14}O_4$ (222.0892)	6	*(structure)*

11	$C_{18}H_{18}O_7$ (346.1053)	10		24	$C_{13}H_{10}O_6$ (262.0477)	9	
12	$C_{10}H_{12}O_3$ (180.0786)	5		25	$C_{13}H_{14}O_4$ (234.0892)	7	
13	$C_7H_6O_4$ (154.0266)	5		26	$C_{14}H_{14}O_5$ (262.0841)	8	
14	$C_{16}H_{18}O_6$ (306.1103)	8		$C_{13}H_{10}O_5$ (246.0528) (No. 5; GUA+DMB POS)			
15	$C_7H_6O_5$ (170.0215)	5		27	$C_{19}H_{16}O_6$ (340.0947)	12	
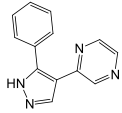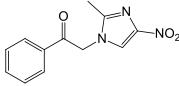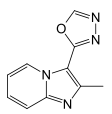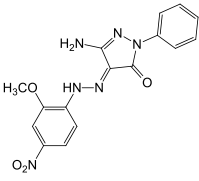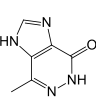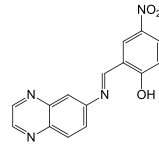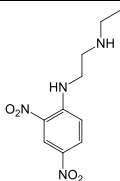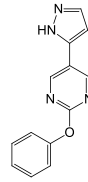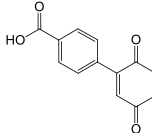
226
227
228
229
230
231
232
233
234
235
236
237
238
239
240
241
242
243
244
245
246
247
248
249
250
251

Table S2. Possible structures of the major products detected from GUA+VL using UHPLC-HESI- Orbitrap-MS operated in positive (POS) and negative (NEG) ion modes.
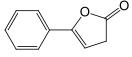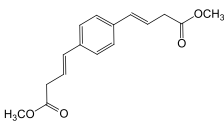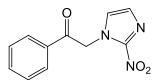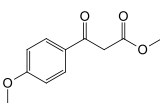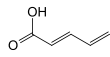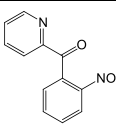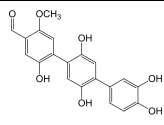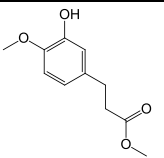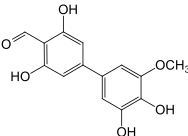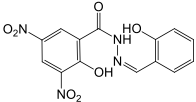
No.	GUA+VL POS Molecular formula and exact mass	DBE	Possible structure	No.	GUA+VL NEG Molecular formula and exact mass	DBE	Possible structure
28	$C_7H_8O_4$ (156.0423)	4	(structure)	35	$C_8H_8O_5$ (184.0372)	5	(structure)
	$C_{13}H_{10}O_4$ (230.0579) (No. 4; GUA+DMB, Table S1)				$C_{13}H_{12}O_4$ (232.0736) (No. 6; GUA+DMB, Table S1)		
	$C_{13}H_{12}O_4$ (232.0736) (No. 6; GUA+DMB, Table S1)				$C_{14}H_{14}O_4$ (246.0892) (No. 1; GUA+DMB, Table S1)		
	$C_{13}H_{10}O_5$ (246.0528) (No. 5; GUA+DMB, Table S1)				$C_{14}H_{14}O_6$ (278.0790) (No. 16; GUA+DMB, Table S1)		
29	$C_7H_8O_5$ (172.0372)	4	(structure)		$C_{20}H_{18}O_6$ (354.1103) (No. 21; GUA+DMB, Table S1)		
30	$C_6H_6O_2$ (110.0368)	4	(structure)		$C_{12}H_{10}O_4$ (218.0579) (No. 17; GUA+DMB, Table S1)		
31	$C_{10}H_{10}O_4$ (194.0579)	6	(structure)		$C_6H_6O_2$ (110.0368) (No. 30; GUA+VL POS)		
32	$C_{11}H_8O_4$ (204.0423)	8	(structure)		$C_7H_{10}O_5$ (174.0528) (No. 18; GUA+DMB, Table S1)		
33	$C_{12}H_{10}O_3$ (202.0630)	8	(structure)	36	$C_{15}H_{14}O_5$ (274.0841)	9	(structure)
	$C_{14}H_{12}O_5$ (260.0685) (No. 7; GUA+DMB, Table S1)				$C_{13}H_{12}O_6$ (264.0634) (No. 20; GUA+DMB, Table S1)		
	$C_{13}H_{14}O_4$ (234.0892) (No. 25; GUA+DMB, Table S1)			37	$C_8H_8O_4$ (168.0423)	5	(structure)
34	$C_{11}H_{10}O_6$ (238.0477)	7	(structure)		$C_{19}H_{16}O_6$ (340.0947) (No. 27; GUA+DMB, Table S1)		
	$C_{13}H_{10}O_6$ (262.0477) (No. 24; GUA+DMB, Table S1)				$C_{11}H_{10}O_6$ (238.0477) (No. 34; GUA+VL POS)		
	$C_{13}H_{12}O_6$ (264.0634) (No. 20; GUA+DMB, Table S1)			38	$C_5H_6O_5$ (146.0215)	3	(structure)
	$C_7H_6O_4$ (154.0266) (No. 13; GUA+DMB, Table S1)			39	$C_6H_4O_4$ (140.0110)	5	(structure)

Table S3. Possible structures of the major products detected from GUA+DMB+AN using UHPLC-HESI-Orbitrap-MS operated in positive (POS) and negative (NEG) ion modes.
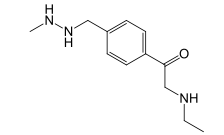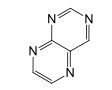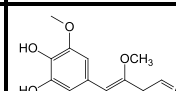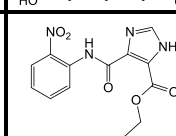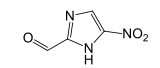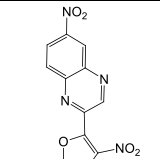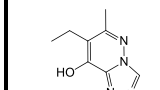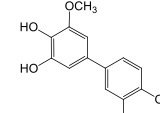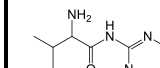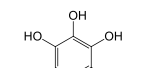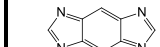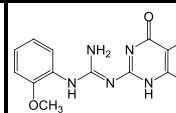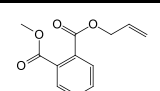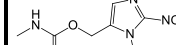
No.	GUA+DMB+AN POS Molecular formula and exact mass	DBE	Possible structure	No.	GUA+DMB +AN NEG Molecular formula and exact mass	DBE	Possible structure
$C_{14}H_{14}O_4$ (246.0892) (No. 1; GUA+DMB, Table S1)				$C_{13}H_{12}O_4$ (232.0736) (No. 6; GUA+DMB, Table S1)			
40	$C_{13}H_{10}N_4$ (222.0905)	11			$C_{14}H_{14}O_6$ (278.0790) (No. 16; GUA+DMB, Table S1)		
$C_{13}H_{10}O_5$ (246.0528) (No. 5; GUA+DMB, Table S1)				$C_{14}H_{14}O_4$ (246.0892) (No. 1; GUA+DMB, Table S1)			
$C_{13}H_{10}O_4$ (230.0579) (No. 4; GUA+DMB, Table S1)				$C_{12}H_{10}O_4$ (218.0579) (No. 17; GUA+DMB, Table S1)			
41	$C_6H_6N_4$ (134.0592)	6			$C_{21}H_{18}O_8$ (398.1002) (No. 19; GUA+DMB, Table S1)		
$C_{13}H_{12}O_4$ (232.0736) (No. 6; GUA+DMB, Table S1)				$C_7H_{10}O_5$ (174.0528) (No. 18; GUA+DMB, Table S1)			
42	$C_{12}H_{11}N_3O_3$ (245.0800)	9			$C_{13}H_{12}O_6$ (264.0634) (No. 20; GUA+DMB, Table S1)		
43	$C_{10}H_8N_4O$ (200.0698)	9		48	$C_{16}H_{14}N_6O_4$ (354.1076)	13	
44	$C_6H_6N_4O$ (150.0542)	6		49	$C_{15}H_{10}N_4O_3$ (294.0753)	13	
45	$C_{10}H_{14}N_4O_4$ (245.1015)	6			$C_{13}H_{10}O_6$ (262.0477) (No. 24; GUA+DMB, Table S1)		
46	$C_{13}H_{10}N_4O$ (238.0855)	11			$C_{10}H_{10}O_4$ (194.0579) (No. 31; GUA+VL, Table S2)		
$C_{13}H_{12}O_6$ (264.0634) (No. 20; GUA+DMB, Table S1)				$C_7H_8O_4$ (156.0423) (No. 28; GUA+VL, Table S2)			
$C_7H_6O_4$ (154.0266) (No. 13; GUA+DMB, Table S1)				$C_{13}H_{14}O_4$ (234.0892) (No. 25; GUA+DMB, Table S1)			
$C_{12}H_{10}O_3$ (202.0630) (No. 33; GUA+VL, Table S2)				$C_{13}H_{10}O_5$ (246.0528) (No. 5; GUA+DMB, Table S1)			
47	$C_{13}H_8O_4$ (228.0423)	10			$C_{14}H_{14}O_5$ (262.0841) (No. 26; GUA+DMB, Table S1)		

Table S4. Possible structures of the major products detected from GUA+VL+AN using
UHPLC-HESI-Orbitrap-MS operated in positive (POS) and negative (NEG) ion modes.

No.	GUA+VL+AN POS Molecular formula and exact mass	DBE	Possible structure	No.	GUA+VL+AN NEG Molecular formula and exact mass	DBE	Possible structure
C$_{14}$H$_{14}$O$_4$ (246.0892) (No. 1; GUA+DMB, Table S1)				C$_{13}$H$_{12}$O$_4$ (232.0736) (No. 6; GUA+DMB, Table S1)			
50	C$_{10}$H$_8$O$_2$ (160.0524)	7		C$_{14}$H$_{14}$O$_6$ (278.0790) (No.16; GUA+DMB, Table S1)			
51	C$_{16}$H$_{18}$O$_4$ (274.1205)	8		C$_{12}$H$_{10}$O$_4$ (218.0579) (No.17; GUA+DMB, Table S1)			
\multicolumn C$_{11}$H$_{12}$O$_5$ (224.0685) (No. 8; GUA+DMB, Table S1)			57	C$_{11}$H$_9$N$_3$O$_3$ (231.0644)	9	
C$_{14}$H$_{12}$O$_5$ (260.068) (No. 7; GUA+DMB, Table S1)				C$_7$H$_{10}$O$_5$ (174.0528) (No.18; GUA+DMB, Table S1)			
C$_{12}$H$_{14}$O$_4$ (222.0892) (No. 23; GUA+DMB, Table S1)				C$_{15}$H$_{14}$O$_5$ (274.0841) (No. 36; GUA+VL, Table S2)			
52	C$_{11}$H$_{12}$O$_4$ (208.0736)	6		C$_{13}$H$_{12}$O$_6$ (264.0634) (No. 20; GUA+DMB, Table S1)			
\multicolumn C$_6$H$_6$N$_4$O (150.0542) (No. 44; GUA+DMB+AN, Table S3)			58	C$_5$H$_6$O$_2$ (98.0368)	3	
C$_{13}$H$_{12}$O$_4$ (232.0736) (No. 6; GUA+DMB, Table S1)				C$_{19}$H$_{16}$O$_6$ (340.0947) (No. 27; GUA+DMB, Table S1)			
53	C$_{12}$H$_8$N$_2$O$_3$ (228.0535)	10		59	C$_{20}$H$_{16}$O$_7$ (368.0896)	13	
54	C$_{11}$H$_{14}$O$_4$ (210.0892)	5		C$_{21}$H$_{18}$O$_8$ (398.1002) (No. 19; GUA+DMB, Table S1)			
C$_7$H$_6$O$_4$ (154.0266) (No. 13; GUA+DMB, Table S1)				C$_7$H$_6$O$_4$ (154.0266) (No. 13; GUA+DMB, Table S1)			
55	C$_{14}$H$_{12}$O$_6$ (276.0634)	9		C$_{15}$H$_{10}$N$_4$O$_3$ (294.0753) (No. 49; GUA+DMB+AN, Table S3)			
56	C$_{14}$H$_{10}$N$_4$O$_7$ (346.0550)	12		C$_{13}$H$_{10}$O$_6$ (262.0477) (No. 24; GUA+DMB, Table S1)			
C$_{13}$H$_{12}$O$_6$ (264.0634) (No. 20; GUA+DMB, Table S1)				C$_5$H$_6$O$_5$ (146.0215) (No. 38; GUA+VL, Table S2)			

Table S5. Possible structures of the major products detected from GUA+AN using UHPLC-
HESI-Orbitrap-MS operated in positive (POS) and negative (NEG) ion modes.

No.	GUA+AN POS Molecular formula and exact mass	DBE	Possible structure	No.	GUA+AN NEG Molecular formula and exact mass	DBE	Possible structure
	$C_{13}H_{10}O_4$ (230.0579) (No. 4; GUA+DMB, Table S1)				$C_{14}H_{14}O_6$ (278.0790) (No. 16; GUA+DMB, Table S1)		
	$C_6H_6N_4O$ (150.0542) (No. 44; GUA+DMB+AN, Table S3)			68	$C_{12}H_{19}N_3O$ (221.1528)	5	
	$C_{11}H_{12}O_5$ (224.0685) (No. 8; GUA+DMB, Table S1)				$C_{12}H_{10}O_4$ (218.0579) (No. 17; GUA+DMB, Table S1)		
	$C_7H_8O_4$ (156.0423) (No. 28; GUA+VL, Table S2)				$C_{14}H_{14}O_4$ (246.0892) (No. 1; GUA+DMB, Table S1)		
60	$C_6H_4N_4$ (132.0436)	7			$C_{20}H_{18}O_6$ (354.1103) (No. 21; GUA+DMB, Table S1)		
61	$C_{12}H_{14}O_5$ (238.0841)	6			$C_7H_{10}O_5$ (174.0528 (No. 18; GUA+DMB, Table S1)		
62	$C_{13}H_{12}N_4O_5$ (304.0808)	10		69	$C_4H_3N_3O_3$ (141.0174)	5	
	$C_{13}H_{12}O_6$ (264.0634) (No. 20; GUA+DMB, Table S1)				$C_{13}H_{12}O_6$ (264.0634) (No. 20; GUA+DMB, Table S1)		
	$C_{13}H_{12}O_4$ (232.0736) (No. 6; GUA+DMB, Table S1)			70	$C_{12}H_6N_4O_5$ (286.0338)	12	
63	$C_8H_{10}N_4O$ (178.0855)	6		71	$C_{13}H_{12}O_5$ (248.0685)	8	
64	$C_9H_{14}N_4O$ (194.1168)	5		72	$C_6H_6O_4$ (142.0266)	4	
65	$C_8H_4N_4$ (156.0436)	9			$C_{12}H_{10}O_3$ (202.0630) (No. 33; GUA+VL, Table S2)		
66	$C_{15}H_{19}N_5O_2$ (301.1539)	9		73	$C_{12}H_{12}O_4$ (220.0736)	7	
67	$C_7H_{10}N_4O_4$ (214.0702)	5			$C_7H_6O_5$ (170.0215) (No. 15; GUA+DMB, Table S1)		
	$C_7H_8O_5$ (172.0372) (No. 29; GUA+VL, Table S2)				$C_7H_8O_4$ (156.0423) (No. 28; GUA+VL, Table S2)		
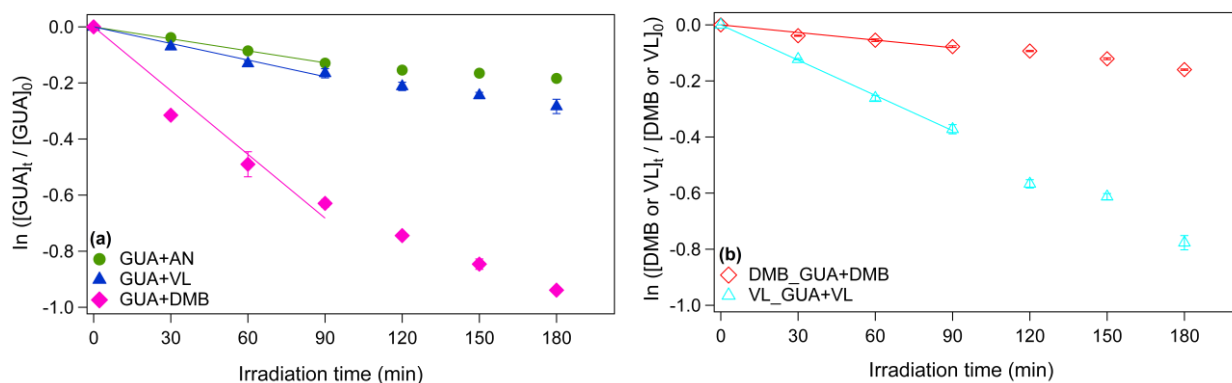
Figure S1. (a) The decay of GUA during (ammonium) nitrate-mediated photo-oxidation (GUA+AN) and photosensitized oxidation by ^{3}VL* (GUA+VL) or ^{3}DMB* (GUA+DMB). (b) The decay of DMB or VL during GUA photo-oxidation in GUA+DMB and GUA+VL, respectively. No statistically significant difference ($p > 0.05$) was noted between GUA+DMB and GUA+DMB+AN and between GUA+VL and GUA+VL+AN. Error bars represent 1 standard deviation; most error bars are smaller than the markers.

305

306
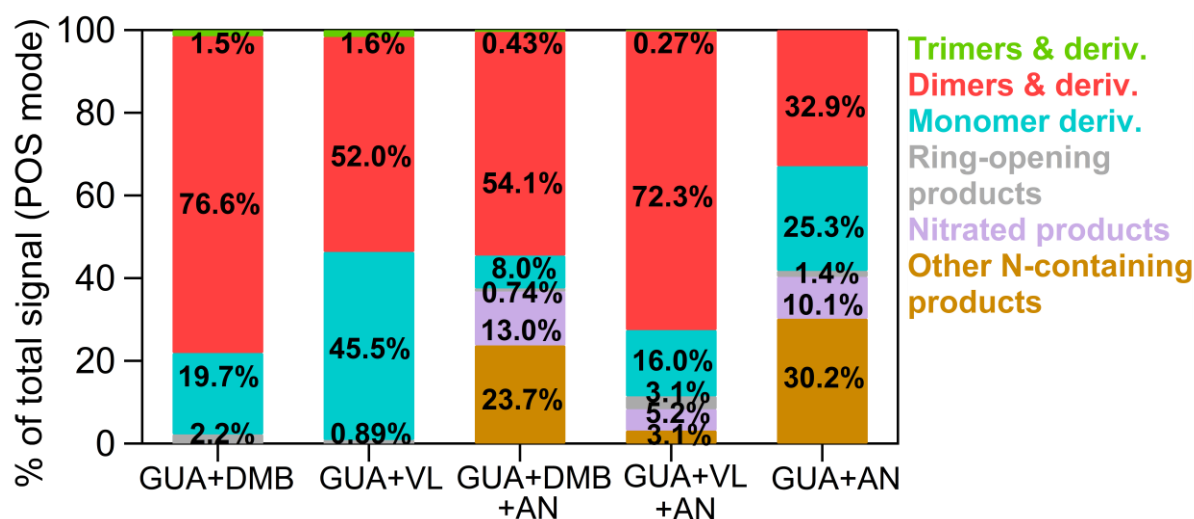
Figure S2. Signal-weighted distributions of aqSOA from GUA+DMB, GUA+VL, GUA+DMB+AN, GUA+VL+AN, and GUA+AN. These product distributions were calculated from UHPLC-HESI-Orbitrap-MS data obtained in the positive (POS) ion mode. The values indicate the contribution of different product classifications to the total signals for each reaction condition.

312
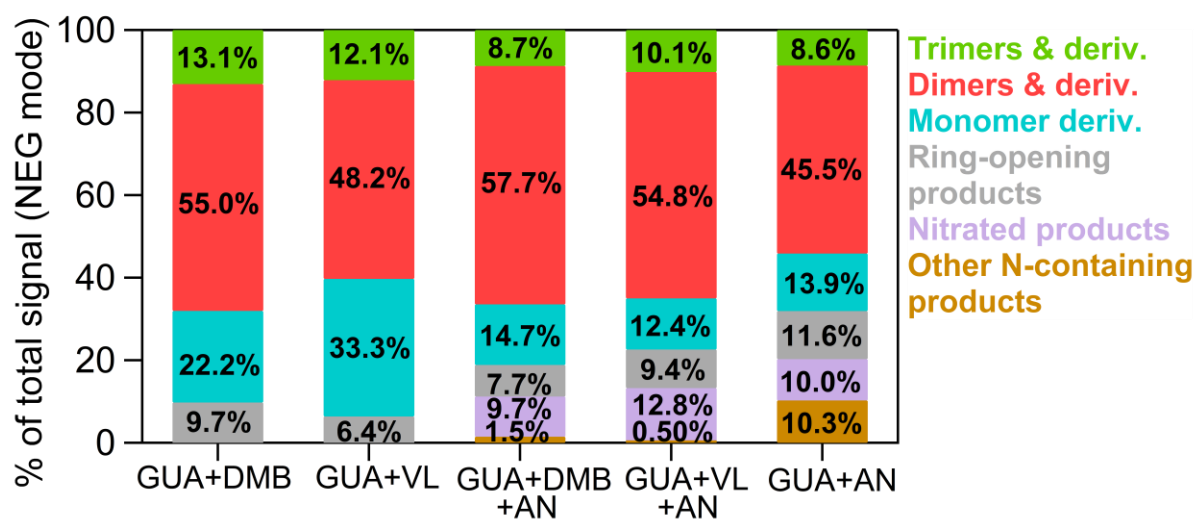
313 **Figure S3.** Signal-weighted distributions of aqSOA from GUA+DMB, GUA+VL, GUA+DMB+AN, GUA+VL+AN, and GUA+AN. These product distributions were calculated from UPLC-HESI-Orbitrap-MS data obtained in the negative (NEG) ion mode. The values indicate the contribution of different product classifications to the total signals for each reaction condition.

318
319
320
321
322

323
324
325
326
327
328
329
330
331
332
333
334
335
336

337
338 **Figure S4.** The concentration of formic, oxalic, and succinic acid for GUA+DMB, GUA+VL,
339 GUA+DMB+AN, and GUA+VL+AN aqSOA. Error bars represent one standard deviation of
340 triplicate experiments.

341

342
343
344
345
346
347
348
349
350
351
352
353
354
355
356
357
358
359
360
361
362
363
364
365
366
367
368

369
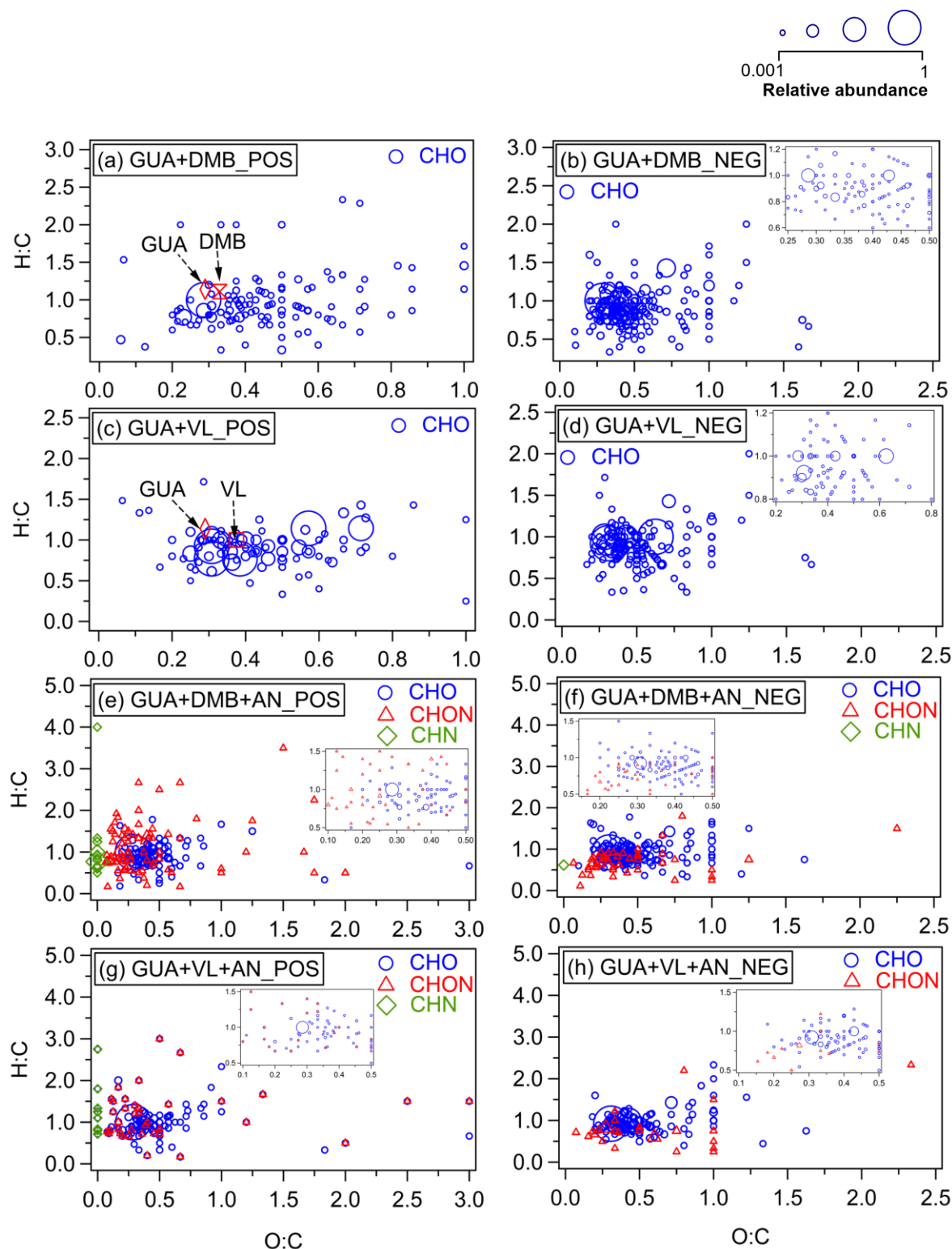
Figure S5. Van Krevelen diagrams of aqSOA from (a, b) GUA+DMB, (c, d) GUA+VL, (e, f) GUA+DMB+AN, and (g, h) GUA+VL+AN for positive (POS) and negative (NEG) ion modes. The blue circle markers indicate CHO classes, red triangle indicate CHON classes, and green diamond indicate CHN classes. The marker size reflects the relative abundance in the sample. The location of GUA, DMB, and VL in the plots are indicated only in panels a and c (red markers). The insets are expanded views of the crowded sections of the van Krevelen diagrams. Note the different scales on the axes.
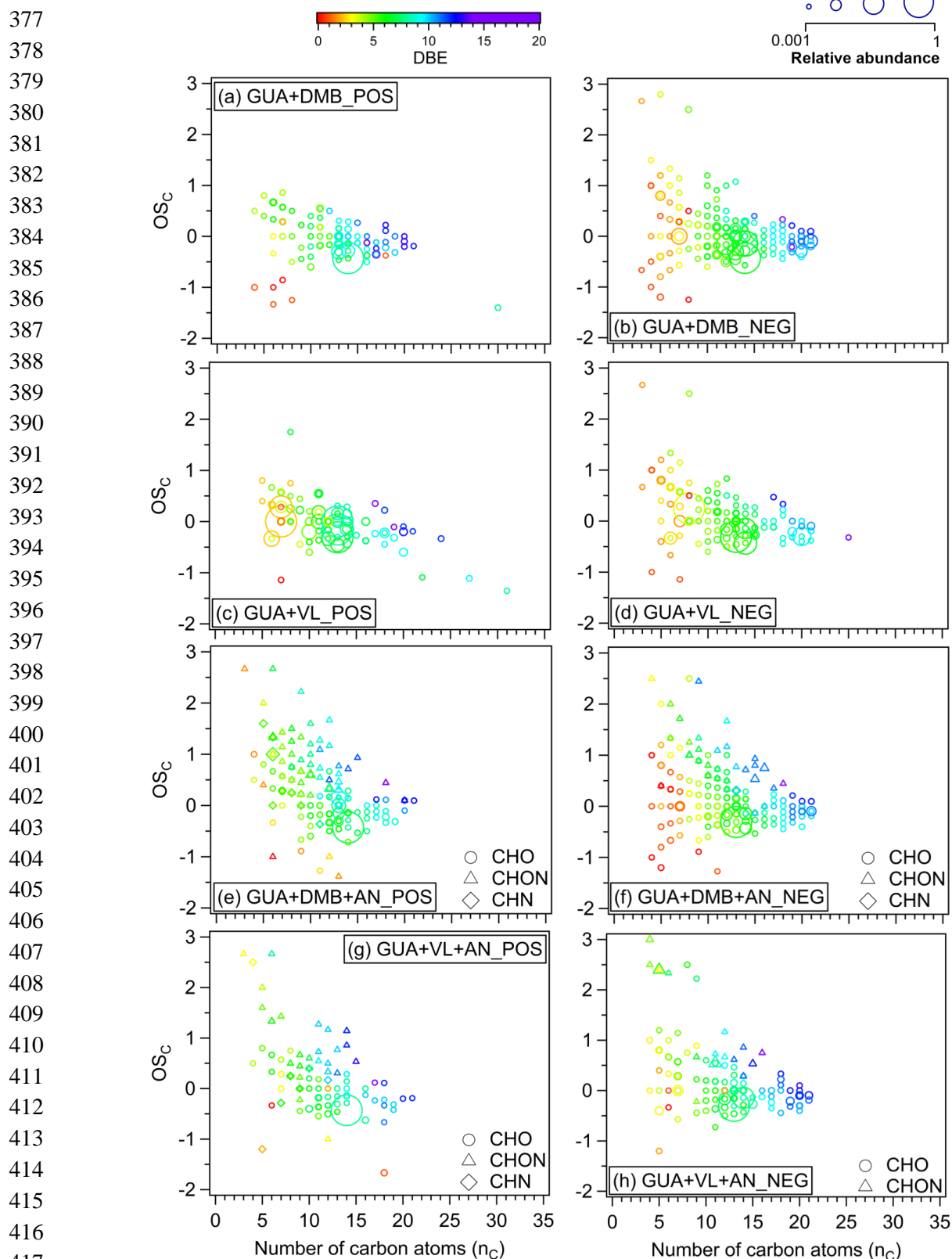
Figure S6. Plots of the carbon oxidation state (OS_C) vs. the number of carbon atoms (n_C) of aqSOA from (a, b) GUA+DMB, (c, d) GUA+VL, (e, f) GUA+DMB+AN, and (g, h) GUA+VL+AN for positive (POS) and negative (NEG) ion modes, colored by the double bond equivalent (DBE) values. The circle, triangle, and diamond markers indicate CHO, CHON and CHN classes, respectively. The marker size reflects the relative abundance in the sample.
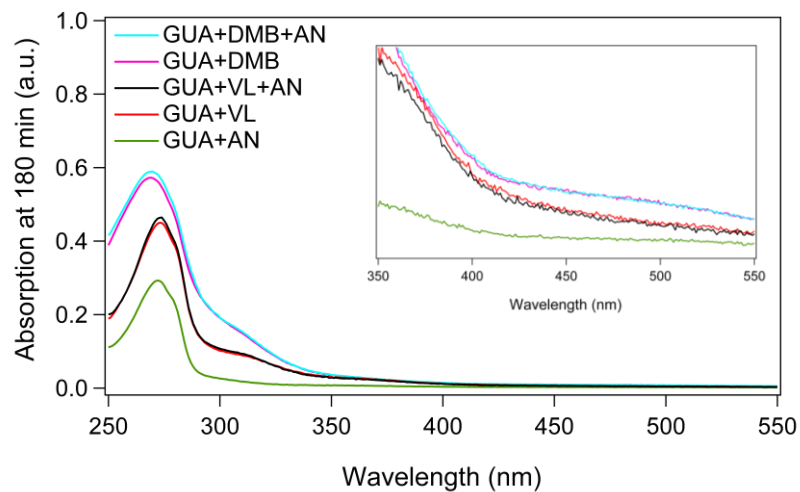
Figure S7. UV-Vis absorption spectra of GUA+DMB+AN, GUA+DMB, GUA+VL+AN, GUA+VL, and GUA+AN after 180 min of irradiation. The inset is the expanded view from 350 to 550 nm.

441
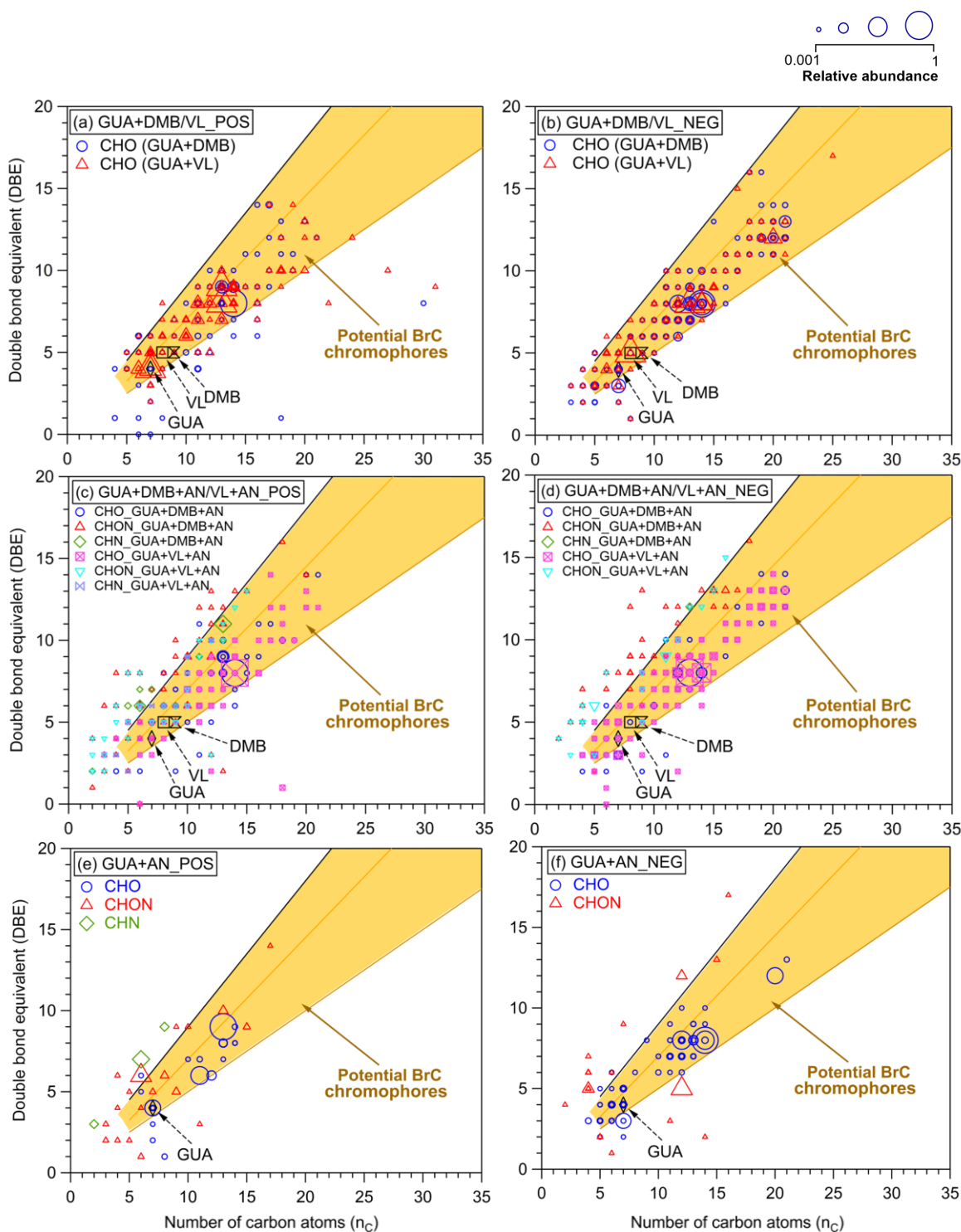
Figure S8. Plots of the double bond equivalent (DBE) values vs. the number of carbon atoms (n_C) (Lin et al., 2018) of aqSOA from (a, b) GUA+DMB and GUA+VL, (c, d) GUA+DMB+AN and GUA+VL+AN, and (e, f) GUA+AN for positive (POS) and negative (NEG) ion modes. For a and b, the blue markers indicate CHO classes for GUA+DMB and red indicate CHO classes for GUA+VL. For c and d, the blue markers indicate CHO classes, red indicate CHON classes, and green indicate CHN classes for GUA+DMB+AN; the pink markers indicate CHO classes, cyan indicate CHON classes, and purple indicate CHN classes for GUA+VL+AN. For e and f, the blue markers indicate CHO classes, red indicate CHON classes, and green indicate

450 CHN classes for GUA+AN. The marker size reflects the relative abundance in the sample. The
451 three lines indicate DBE reference values of fullerene-like hydrocarbons (top, black solid line;
452 Lobodin et al, 2012), cata-condensed polycyclic aromatic hydrocarbons (PAHs; Siegmann and
453 Sattler, 2000) (middle, orange solid line), and linear conjugated polyenes (general formula
454 C_xH_{x+2}) (bottom, brown solid line). Species within the shaded area are potential BrC
455 chromophores.
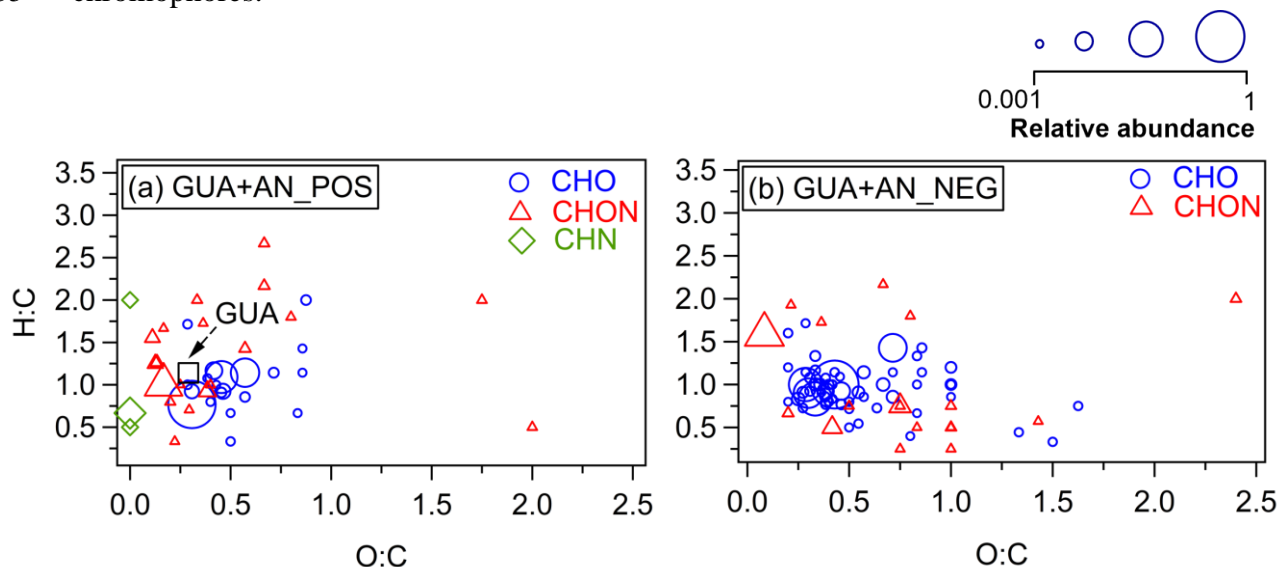
456 **Figure S9.** Van Krevelen diagrams of aqSOA from GUA+AN for (a) positive (POS) and (b)
457 negative (NEG) ion modes. The blue markers indicate CHO classes, red indicate CHON
458 classes, and green indicate CHN classes. The marker size reflects the relative abundance in the
459 sample. The location of GUA is indicated only in panel a (black marker).
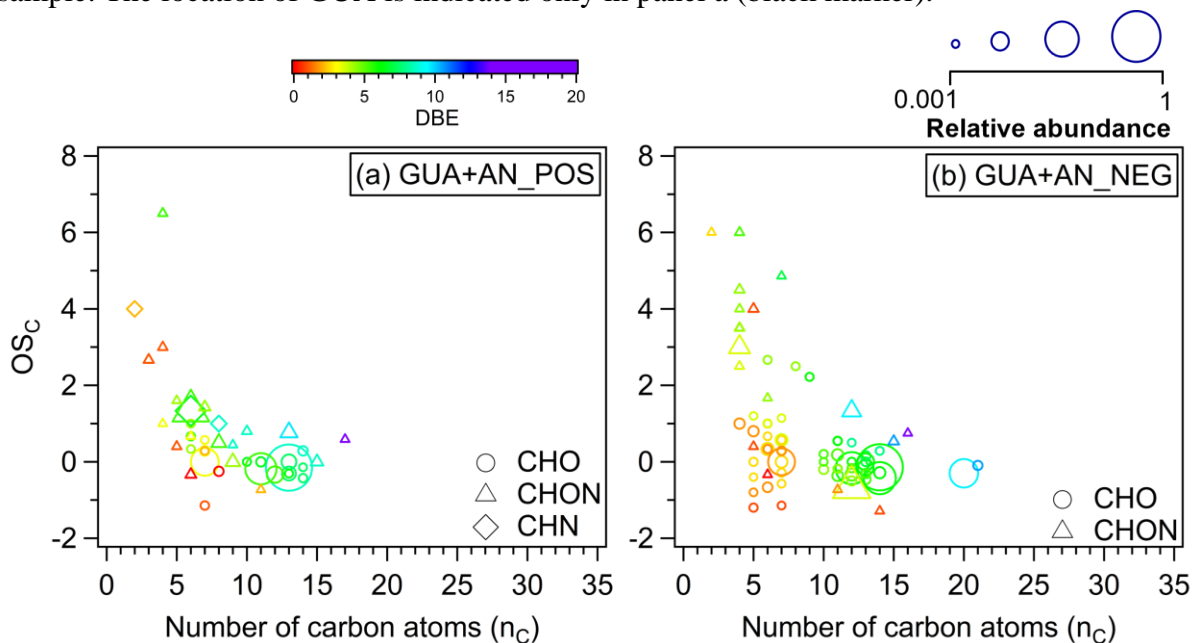
460
461 **Figure S10**. Plots of the carbon oxidation state (OS_C) vs. the number of carbon atoms (n_C) of
462 aqSOA from GUA+AN for (a) positive (POS) and (b) negative (NEG) ion modes, colored by
463 the double bond equivalent (DBE) values. The circle, triangle, and diamond markers indicate
464 CHO, CHON and CHN classes, respectively. The marker size reflects the relative abundance
465 in the sample.

References

Anastasio, C., Faust, B. C., and Rao, C. J.: Aromatic carbonyl compounds as aqueous-phase photochemical sources of hydrogen peroxide in acidic sulfate aerosols, fogs, and clouds. 1. Non-phenolic methoxybenzaldehydes and methoxyacetophenones with reductants (phenols), Environ. Sci. Technol., 31, 218−232, https://doi.org/10.1021/es960359g, 1997.

Bateman, A. P., Laskin, J., Laskin, A., and Nizkorodov, S. A.: Applications of high-resolution electrospray ionization mass spectrometry to measurements of average oxygen to carbon ratios in secondary organic aerosols, Environ. Sci. Technol., 46, 8315–832, https://doi.org/10.1021/es3017254, 2012.

Chen, Y., Li, N., Li, X., Tao, Y., Luo, S., Zhao, Z., Ma, S., Huang, H., Chen, Y., Ye, Z., and Ge, X.: Secondary organic aerosol formation from $^3C^*$-initiated oxidation of 4-ethylguaiacol in atmospheric aqueous-phase, Sci. Total Environ., 723, 137953, https://doi.org/10.1016/j.scitotenv.2020.137953, 2020.

Claeys, M., Vermeylen, R., Yasmeen, F., Gómez-González, Y., Chi, X., Maenhaut, W., Mészáros, T., and Salma, I.: Chemical characterization of humic-like substances from urban, rural and tropical biomass burning environments using liquid chromatography with UV/vis photodiode array detection and electrospray ionization mass spectrometry, Environ. Chem., 9, 273–284, https://doi.org/10.1071/EN11163, 2012.

He, L., Schaefer, T., Otto, T., Kroflič, A., and Herrmann, H.: Kinetic and theoretical study of the atmospheric aqueous-phase reactions of OH radicals with methoxyphenolic compounds, J. Phys. Chem. A, 123, 7828−7838, https://doi.org/10.1021/acs.jpca.9b05696, 2019.

Jiang, W., Misovich, M. V., Hettiyadura, A. P. S., Laskin, A., McFall, A. S., Anastasio, C., and Zhang, Q.: Photosensitized reactions of a phenolic carbonyl from wood combustion in the aqueous phase—chemical evolution and light absorption properties of aqSOA, Environ. Sci. Technol., 55, 5199−5211, https://doi.org/10.1021/acs.est.0c07581, 2021.

Koch, B. P. and Dittmar, T.: From mass to structure: an aromaticity index for high-resolution mass data of natural organic matter, Rapid Commun. Mass Spectrom., 20, 926–932, https://doi.org/10.1002/rcm.2386, 2006.

Kourtchev, I., Godoi, R. H. M., Connors, S., Levine, J. G., Archibald, A. T., Godoi, A. F. L., Paralovo, S. L., Barbosa, C. G. G., Souza, R. A. F., Manzi, A. O., Seco, R., Sjostedt, S., Park, J., Guenther, A., Kim, S., Smith, J., Martin, S. T., and Kalberer, M.: Molecular composition of organic aerosols in central Amazonia: an ultra-high-resolution mass spectrometry study, Atmos. Chem. Phys., 16, 11899–11913, https://doi.org/10.5194/acp-16-11899-2016, 2016.

Kroll, J. H., Donahue, N. M., Jimenez, J. L., Kessler, S. H., Canagaratna, M. R., Wilson, K. R., Altieri, K. E., Mazzoleni, L. R., Wozniak, A. S., Bluhm, H., Mysak, E. R., Smith, J. D., Kolb, C. E., and Worsnop, D. R.: Carbon oxidation state as a metric for describing the chemistry of atmospheric organic aerosol, Nat. Chem., 3, 133–139, https://doi.org/10.1038/nchem.948, 2011.

Kroll, J. H., Lim, C. Y., Kessler, S. H., and Wilson, K. R.: Heterogeneous oxidation of atmospheric organic aerosol: kinetics of changes to the amount and oxidation state of particle-

phase organic carbon, J. Phys. Chem. A, 119, 10767−10783, https://doi.org/10.1021/acs.jpca.5b06946, 2015.

Laskin, J., Laskin, A., Nizkorodov, S. A., Roach, P., Eckert, P., Gilles, M. K., Wang, B., Lee, H. J., and Hu, Q.: Molecular selectivity of brown carbon chromophores, Environ. Sci. Technol., 48, 12047–12055, https://doi.org/10.1021/es503432r, 2014.

Li, Y. J., Huang, D. D., Cheung, H. Y., Lee, A. K. Y., and Chan, C. K.: Aqueous-phase photochemical oxidation and direct photolysis of vanillin - a model compound of methoxy phenols from biomass burning, Atmos. Chem. Phys., 14, 2871−2885, https://doi.org/10.5194/acp-14-2871-2014, 2014.

Lin, P., Fleming, L. T., Nizkorodov, S. A., Laskin, J., and Laskin, A.: Comprehensive molecular characterization of atmospheric brown carbon by high resolution mass spectrometry with electrospray and atmospheric pressure photoionization, Anal. Chem., 90, 12493–12502, https://doi.org/10.1021/acs.analchem.8b02177, 2018.

Lobodin, V. V., Marshall, A. G., and Hsu, C. S.: Compositional space boundaries for organic compounds, Anal. Chem., 84, 3410–3416, https://doi.org/10.1021/ac300244f, 2012.

Lv, J., Zhang, S., Luo, L., and Cao, D.: Solid-phase extraction-stepwise elution (SPE-SE) procedure for isolation of dissolved organic matter prior to ESI-FT-ICR-MS analysis, Anal. Chim. Acta, 948, 55−61, https://doi.org/10.1016/j.aca.2016.10.038, 2016.

Mabato, B. R. G., Lyu, Y., Ji, Y., Li, Y. J., Huang, D. D., Li, X., Nah, T., Lam, C. H., and Chan, C. K.: Aqueous secondary organic aerosol formation from the direct photosensitized oxidation of vanillin in the absence and presence of ammonium nitrate, Atmos. Chem. Phys., 22, 273−293, https://doi.org/10.5194/acp-22-273-2022, 2022.

Misovich, M. V., Hettiyadura, A. P. S., Jiang, W., Zhang, Q., and Laskin, A.: Molecular-level study of the photo-oxidation of aqueous-phase guaiacyl acetone in the presence of ^{3}C*: formation of brown carbon products, ACS Earth Space Chem., 5, 1983−1996, https://doi.org/10.1021/acsearthspacechem.1c00103, 2021.

Schmitt-Kopplin, P., Gelencsér, A., Dabek-Zlotorzynska, E., Kiss, G., Hertkorn, N., Harir, M., Hong, Y., and Gebefügi, I.: Analysis of the unresolved organic fraction in atmospheric aerosols with ultrahigh–resolution mass spectrometry and nuclear magnetic resonance spectroscopy: organosulfates as photochemical smog constituents, Anal. Chem., 82, 8017–8026, https://doi.org/10.1021/ac101444r, 2010.

Siegmann, K. and Sattler, K.: Formation mechanism for polycyclic aromatic hydrocarbons in methane flames, J. Chem. Phys., 112, 698–709, https://doi.org/10.1063/1.480648, 2000.

Smith, J. D., Sio, V., Yu, L., Zhang, Q., and Anastasio, C.: Secondary organic aerosol production from aqueous reactions of atmospheric phenols with an organic triplet excited state, Environ. Sci. Technol., 48, 1049–1057, https://doi.org/10.1021/es4045715, 2014.

Smith, J. D., Kinney, H., and Anastasio, C.: Phenolic carbonyls undergo rapid aqueous photodegradation to form low-volatility, light-absorbing products, Atmos. Environ., 126, 36−44, https://doi.org/10.1016/j.atmosenv.2015.11.035, 2016.

566   Yee, L. D., Kautzman, K. E., Loza, C. L., Schilling, K. A., Coggon, M. M., Chhabra, P. S.,
567   Chan, M. N., Chan, A. W. H., Hersey, S. P., Crounse, J. D., Wennberg, P. O., Flagan, R. C.,
568   and Seinfeld, J. H.: Secondary organic aerosol formation from biomass burning intermediates:
569   phenol and methoxyphenols, Atmos. Chem. Phys., 13, 8019–8043,
570   https://doi.org/10.5194/acp- 13-8019-2013, 2013.

572   Yu, L., Smith, J., Laskin, A., Anastasio, C., Laskin, J., and Zhang, Q.: Chemical
573   characterization of SOA formed from aqueous-phase reactions of phenols with the triplet
574   excited state of carbonyl and hydroxyl radical, Atmos. Chem. Phys., 14, 13801−13816,
575   https://doi.org/10.5194/acp-14-13801-2014, 2014.

577   Yu, L., Smith, J., Laskin, A., George, K. M., Anastasio, C., Laskin, J., Dillner, A. M., and
578   Zhang, Q.: Molecular transformations of phenolic SOA during photochemical aging in the
579   aqueous phase: competition among oligomerization, functionalization, and fragmentation,
580   Atmos. Chem. Phys., 16, 4511−4527, https://doi.org/10.5194/acp-16-4511-2016.